

PCT/GB 2003 / 0 0 5 3 9 5

Rec'd PCT/10 13 JUN 2005

10/538316

INVESTOR IN PEOPLE



**PRIORITY
DOCUMENT**
SUBMITTED OR TRANSMITTED IN
COMPLIANCE WITH RULE 17.1(a) OR (b)

The Patent Office
Concept House
Cardiff Road
Newport
South Wales
NP10 8QQ

REC'D 05 FEB 2004

WIPO PCT

I, the undersigned, being an officer duly authorised in accordance with Section 74(1) and (4) of the Deregulation & Contracting Out Act 1994, to sign and issue certificates on behalf of the Comptroller-General, hereby certify that annexed hereto is a true copy of the documents as originally filed in connection with the patent application identified therein.

In accordance with the Patents (Companies Re-registration) Rules 1982, if a company named in this certificate and any accompanying documents has re-registered under the Companies Act 1980 with the same name as that with which it was registered immediately before re-registration save for the substitution as, or inclusion as, the last part of the name of the words "public limited company" or their equivalents in Welsh, references to the name of the company in this certificate and any accompanying documents shall be treated as references to the name with which it is so re-registered.

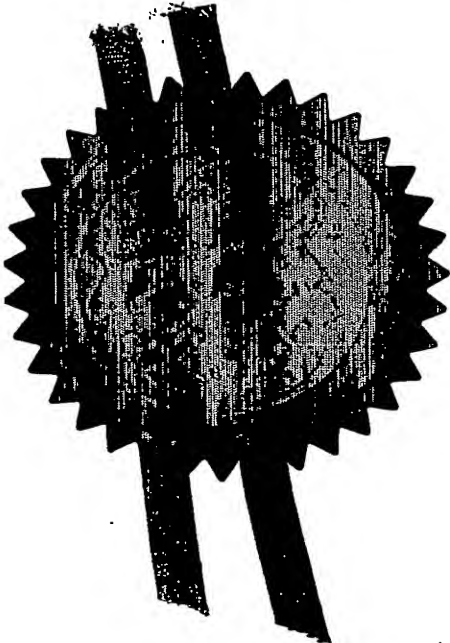
In accordance with the rules, the words "public limited company" may be replaced by p.l.c., plc, P.L.C. or PLC.

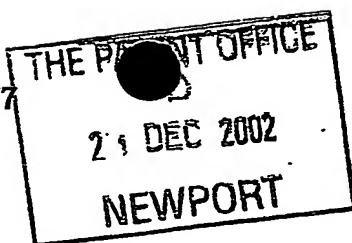
Re-registration under the Companies Act does not constitute a new legal entity but merely subjects the company to certain additional company law rules.

Signed

[Signature]

Dated 21 January 2004





The
Patent
Office

27DEC02 E773311-1.002831
P01/7700 0.00-0229991.5

Request for grant of a patent

(See the notes on the back of this form. You can also get an explanatory leaflet from the Patent Office to help you fill in this form)

The Patent Office

Cardiff Road
Newport
South Wales
NP9 1RH

1. Your reference

57.0474 GB NP

2. Patent application number

(The Patent Office will fill in this part)

21 DEC 2002

0229991.5

3. Full name, address and postcode of the or of each applicant (underline all surnames)

Schlumberger Holdings Limited
P.O. Box 71
Craigmuir Chambers
Road Town
Tortola
British Virgin Islands

04236326001

Patents ADP number (if you know it)

If the applicant is a corporate body, give the country/state of its incorporation

British Virgin Islands

4. Title of the invention

SYSTEM AND METHOD FOR REPRESENTING AND PROCESSING AND
MODELING SUBTERRANEAN SURFACES

5. Name of your agent (if you have one)

"Address for service" in the United Kingdom to which all correspondence should be sent (including the postcode)

William L WANG
Intellectual Property Law Department
Schlumberger Cambridge Research Limited
High Cross
Maddingley Road
Cambridge CB3 0EL
United Kingdom

Patents ADP number (if you know it)

08286361001

6. If you are declaring priority from one or more earlier patent applications, give the country and the date of filing of the or of each of these earlier applications and (if you know it) the or each application number

Country

Priority application number
(if you know it)

Date of filing
(day / month / year)

7. If this application is divided or otherwise derived from an earlier UK application, give the number and the filing date of the earlier application

Number of earlier application

Date of filing
(day / month / year)

8. Is a statement of inventorship and of right to grant of a patent required in support of this request? (Answer 'Yes' if:

YES

- a) any applicant named in part 3 is not an inventor, or
 - b) there is an inventor who is not named as an applicant, or
 - c) any named applicant is a corporate body.
- See note (d))

Patents Form 1/77

9. Enter the number of sheets for any of the following items you are filing with this form. Do not count copies of the same document

Continuation sheets of this form	-
Description	93
Claim(s)	11
Abstract	1
Drawing(s)	28

10. If you are also filing any of the following, state how many against each item.

Priority documents	-
Translations of priority documents	-
Statement of inventorship and right to grant of a patent (<i>Patents Form 7/77</i>)	1 (plus 2 copies)
Request for preliminary examination and search (<i>Patents Form 9/77</i>)	1
Request for substantive examination (<i>Patents Form 10/77</i>)	1
Any other documents (<i>please specify</i>)	-

11. I/We request the grant of a patent on the basis of this application.

Signature	Date
	20 December 2002

12. Name and daytime telephone number of person to contact in the United Kingdom
- William L Wang
01223 325268

Warning

After an application for a patent has been filed, the Comptroller of the Patent Office will consider whether publication or communication of the invention should be prohibited or restricted under Section 22 of the Patents Act 1977. You will be informed if it is necessary to prohibit or restrict your invention in this way. Furthermore, if you live in the United Kingdom, Section 23 of the Patents Act 1977 stops you from applying for a patent abroad without first getting written permission from the Patent Office unless an application has been filed at least 6 weeks beforehand in the United Kingdom for a patent for the same invention and either no direction prohibiting publication or communication has been given, or any such direction has been revoked.

Notes

- If you need help to fill in this form or you have any questions, please contact the Patent Office on 0645 500505.
- Write your answers in capital letters using black ink or you may type them.
- If there is not enough space for all the relevant details on any part of this form, please continue on a separate sheet of paper and write "see continuation sheet" in the relevant part(s). Any continuation sheet should be attached to this form.
- If you have answered 'Yes' Patents Form 7/77 will need to be filed.
- Once you have filled in the form you must remember to sign and date it.
- For details of the fee and ways to pay please contact the Patent Office.

DUPLICATE

System and Method for Representing and Processing and
Modeling Subterranean Surfaces

FIELD OF THE INVENTION:

5 The present invention relates to the field of earth
models for subterranean surfaces. In particular, the
invention relates to systems and methods for improved
representations and processing techniques for
subterranean earth surfaces in earth models used in the
10 exploration and production of hydrocarbon reservoirs.

BACKGROUND OF THE INVENTION:

 In the field of processing earth model data for use
in the extraction of hydrocarbons from the earth,
15 significant resources have been invested in creating
functionality and stabilizing the software quality of
modeling technology. The efforts have been based on
faceted representations, and in particular triangulated
surface methods. However, there are number of key
20 problems associated with extending triangulated surface
methods.

 1. Sampling a smooth surface discretely, for
example with points arranged in a triangle mesh, is
inherently inefficient. In contrast, smooth surfaces can
25 be represented as a Taylor series or as an eigen-function
expansion, e.g., Fourier series of some form. An eigen-
function expansion can be used to compute an algebraic
expression to evaluate normal fields, tangent fields,
etc. This is inherently more compact and efficient than a
30 2D or 3D sampling lattice with some sort of
interpolation.

2. The lack of differentiation makes calculation of a triangulated surface intersection algorithm numerically delicate.

3. Triangles can be used to define shape, but triangles do not efficiently convey an intuitive sense of shape. High resolution and high sampling density make the problem more difficult.

4. Low efficiency triangulation forces application developers to either worry about memory management or to curb flexibility of data set processing.

5. Efficient management of large models means localizing change. It is possible in principle to develop localization methods using triangulated surface models but there are numerical stability issues seen in reference to intersection.

SUMMARY OF THE INVENTION:

Thus, it is an object of the present invention to provide an improved system and method for processing data used for hydrocarbon extraction.

Advantageously the invention allows for improved memory and CPU efficiency of implicit surface construction and editing algorithms.

According to the invention a method is provided for processing data used for hydrocarbon extraction from the earth. The method includes the following steps. Receiving sampled data representing earth structures. Identifying one more symmetry transformation groups from the sampled data. Identifying a set of critical points from the sampled data. Generating a plurality of subdivisions of shapes, the subdivisions together representing the earth structures, the generation being based at least in part on the set of identified critical

points and the symmetry transformation groups. Processing earth model data using the generated subdivision of shapes. And, altering activity relating to extraction of hydrocarbons from a hydrocarbon reservoir based on the processed earth model data.

The identified symmetry transformation group is preferably a set of diffeomorphisms that act on a topologically closed and bounded region in space-time such that under transformation the region occupies the same points in space.

The identified symmetry transformation groups preferably correspond to a plurality of shape families, each of which includes a set of predicted critical points. The subdivisions are preferably generated such that a shape family is selected from the plurality of shape families that corresponds to the identified symmetry transformation group. The selection is preferably being based on closeness of correspondence between the identified critical points from the sampled data and the predicted critical points of the selected shape family.

Each shape family preferably has an associated set of symmetry transformation group orbits, with each orbit being associated with orbit information that specifies whether the orbit contains a predicted critical point and value of the Gaussian curvature of a point in the orbit. The orbit information from the set of symmetry transformation group orbits associated with the selected shape family is preferably applied to the sampled data thereby generating a unique specification of a shape from the selected shape family. Each of the plurality of subdivisions of shapes is preferably generated by

identifying a part of the uniquely specified shape that corresponds to the sampled data. The identified parts are assembled, thereby generating a representation of the earth structures.

5 The plurality of subdivisions are preferably generated such that the number of parameters in each subdivision times the number of subdivisions is substantially less than would be needed using a faceted representation method, and the plurality of subdivisions
10 is more numerically stable than third order or higher representation.

 The invention is also embodied in a system for improved extraction of hydrocarbons from the earth, and in a computer readable medium capable of causing a
15 computer system to carry out steps for processing data relating to earth structures for the extraction of hydrocarbons.

BRIEF DESCRIPTION OF THE DRAWINGS:

20

 Figure 1 shows an open surface and its embedding in a closed surface;

 Figure 2 shows a salt mass's steep flanks and overhangs;

25 Figure 3 shows an example of a 4D representation of a field in Turkmanistan;

 Figure 4 is an image of the MacKenzie River Delta;

 Figure 5 shows some combinations of involved spherical harmonic polynomials, presented in spherical
30 polar coordinates;

 Figure 6 illustrates that in most cases a surface evolves under mcf to a point;

Figures 7a-f forms a series of six images showing
vpmcf suppressing noise;

Figure 8 illustrates the orthogonality condition of
the theorem proposed by Athanassenas;

5 Figure 9 is an aerial image of part of Big Bend
National Park, showing the approximation of a plateau to
a characteristic length scale cone;

Figure 10 is a side view of a noise cone structure;

10 Figure 11 is a satellite image of the Labrador
Trough;

Figure 12 shows s a sequence of folded sediment on
the coast of the Gulf of Oman;

Figure 13 is an image illustrating progressive
flattening of an overburden covering a large salt
15 intrusion;

Figure 14 is a diagram illustrating the Morse
theoretical cell decomposition for a simple configuration
of a capped and bent cylinder;

20 Figures 15-17 show diagrams to aid in the
understanding of the bulls eye construction;

Figure 18 shows two views of an example of a monkey
saddle;

Figure 19a shows the Reeb graph of a standard torus;

25 Figure 19b schematically illustrates a 2D cell
suspension that is induced from the axes and planes of
symmetry and critical point theory;

Figure 20 is cross section of the torus shown in
Figure 19a;

30 Figure 21 is a schematic of the shape synopsis
diagram of the torus shown in Figure 19a;

Figure 22 is a cyclide that is shaded according to
Gaussian and mean curvature;

Figure 23a is a bi-torus with its associated REEB diagram;

Figure 23b is the visual representation of the bi-torus shape synopsis diagram;

5 Figure 24 is a diagram of the octree with a coarse level and leaf level shape index relationship indicated;

The Figure 25 is a diagram shows part of the French model;

10 Figure 26 is an image of the topography of Crater Lake, Oregon;

Figure 27 shows a salt weld in the Gulf of Mexico;

Figures 28a-c illustrate an example of the misfit reduction process;

15 Figures 29a-c illustrates an example of blending a non-differentiable join of two collars;

Figure 30 shows as a geological example a water breach as indicated by the white arrow;

Figure 31 is a NASA Shuttle Mission photograph of the Richat Structure in Mauritania;

20 Figure 32 shows the natural analog to a conformal grid with a proportionally spaced correlation scheme;

Figure 33 illustrates a non-conformal 3D Cartesian grid;

25 Figure 34 is an image of the Devil's Potholes, South Africa;

Figure 35 is an image of the Yukon River delta;

Figures 36a and 36b show, for reference, the background Zechstein Salt and the region in the Zechstein where the vsp was acquired;

30 Figure 37 show the frame graph that ties the vsp region of interest to the Zechstein Salt background;

Figures 38a, 38b, 39a and 39b illustrate the separation of faulted sediments from unfaulted sediments;

Figure 40 illustrates a time-lapse seismic evolution;

5 Figure 41 shows the reference structure for spatial frames to define a topology graph;

Figure 42 is a schematic illustration of the definition of the variables in the mean curvature estimator;

10 Figure 43 is an image of the regularly sampled input surface representing the present example of the top of the salt, rendered by drawing a subset of evenly spaced inlines and crosslines;

Figure 44 shows the surface when re-sampled by interpolating missing sample points;

15 Figure 45 shows the re-sampled surface after 25 iterations of smoothing;

Figure 46 shows the shape index map for the re-sampled surface after 25 iterations of smoothing;

20 Figure 47 shows that there are 33 shapes in the example shown in Figure 46;

Figure 48 is a schematic illustration of a system for improved extraction of hydrocarbons from the earth, according a preferred embodiment of the invention;

25 Figure 49 shows further detail of a data processor according to preferred embodiments of the invention;

Figure 50 shows steps in a method for processing data used for hydrocarbon extraction from the earth, according to preferred embodiments of the invention; and

30 Figure 51 shows further detail of steps in generating an efficient and robust subdivision of shapes, according to preferred embodiments of the invention.

DETAILED DESCRIPTION OF THE INVENTION:

While Low-level curvature-based methods as applied to implicit surfaces are relatively complicated to develop, they do not suffer numerical stability problems. By comparison, on a smooth Riemannian manifold the 3rd derivatives of the square of the signed distance function describes the norm of the 2nd Fundamental Form and the mean curvature. For triangulated surfaces, this result is difficult to apply, because numerical evaluation of 3rd derivatives is not guaranteed to be numerically stable.

According to the invention, differential geometry methods of surface representation will now be described. Many geoscience phenomena are related to some form of fluid flow. If the fluid phenomena under study involve surface tension, then mean curvature flow (mcf) and variants such as volume preserving mean curvature flow (vp-mcf) are accurate modeling tools. (For those unfamiliar with mean curvature flow, imagine the fluid front moving normal to each particle of the fluid front.) The behavior of mcf and vp-mcf are well understood when either is applied to a smooth convex surface, star-shaped surface, a surface of rotation, or an entire graph.

A reservoir structural framework does not seem to be an ideal input to mcf, because noise levels degrade the accuracy of analytical approximations and framework surfaces in general are not well approximated as convex, star-shaped, etc. This perception is erroneous. Our investigation of curvature-based modeling shows that mcf can be used to semi-automate its own noise suppression. Given smooth surface data, according to the invention a method is provided to decompose that surface into a

connected sum of star-shaped or entire graph or axisymmetric surface patches.

The mathematical foundation of mcf is substantial, so we seek a unified mathematical description of shape and its evolution. The concept of a fibre bundle is satisfactory. Nakahara presents a formal definition of a fibre bundle. Standard examples of fibre bundles are vector fields, e.g., velocity fields, and tensor fields, e.g., stress fields and elastic fields, evaluated over a sub-volume. In classical differential geometry, curvature properties of surfaces are economically studied in a fibre bundle setting. We have found that a 4D fibre bundle representation of a reservoir framework is no more difficult to write down than is a 3D fibre bundle representations. The economy of mathematical representation is attractive now from the research view. It will be attractive from the engineering view, since reuse of concepts limits the amount of technology that must be mastered.

The fibre bundle representation of a surface of revolution has the following parts.

1. A base that is homeomorphic to a loop, e.g., a circle, an ellipse, or a polygonal closed curve.
2. A typical fibre that is homeomorphic to a compact connected part of either a conic section or a polygonal line.
3. A structure-group that is a group of diffeomorphisms that smoothly deforms any instance of the typical fibre to any other instance.

Here are a few shapes that are frequently encountered in earth modeling represented as fibre bundles.

5 a. A torus has a circle base and a circle typical fibre. Its structure group is the rotation group $SO(3)$.

10 b. A cyclide is a torus, but the structure group is the rotation group extended by the scale factor diagonal group. Intuitively, it is a skewed torus.

15 c. Any compact planar region R with a polygonal boundary ∂R has a natural bundle structure. To see this, compute the region's bounding box B and embed R in B . (Think of B as a solid.) If there exists a part of ∂R that does not intersect any of the box faces, then attach a skirt S of normal rays to ∂ . Then S , R , and ∂B enclose a sub-volume V .

20 We have found that V is the preferred bundle. The base of the bundle is ∂R and a typical fibre is a polygonal line. The region R is formed from the rotation of a line segment emanating from the centroid of R and joined to the boundary ∂R . The length of the fibre changes instantaneously. The structure group is the
25 Euclidean group of rigid body transformations. The following diagram summarizes this construction.

30 Figure 1 shows on the left an open surface, i.e. a surface that does not enclose space; on the right, a closed region (the large box) is subdivided by the same surface forming an internal boundary. Figure 2 shows a salt mass's steep flanks and overhangs, it also shows an example of the cyclide shape in depth imaging. This is an

example that challenges existing commercial software. WesternGeco commercial processing used to construct this velocity model has the common limitation of accepting single z-valued ("height field") data only. According to the invention we describe below a set of planes in the volume of interest such that a multiple z-value body can be subdivided into sections such that each section is single valued with respect to one of the planes. In other words, each plane parameterizes a section of the reference multi z-valued surface. Each of these planes are equipped with a rotation matrix and translation vector so that the application can orient the surface section so that it appears to be single valued with respect to one of the coordinate planes. (It may be that the rotated and translated section is normal to the (x,y) coordinate plane, which is frequently unacceptable to grid-based applications.)

Material properties of a volume of earth can change during an evolutionary process. The time scale of the evolution can vary from wall clock to calendar to geological record. According to the invention, an evolutionary process is represented using a generalization of the fibre bundle method that is employed for shape. This representation is called an "evolutionary process". Here are its components.

1. The base is a line with period λ_B . A trajectory on the base serves as a clock. The trajectory's sampling increment has units that are appropriate to wall clock sampling, calendar sampling, or geological record sampling.

2. A trajectory has compact support. This means that the process is defined on a closed at the beginning and open at the end bounded interval of the helicoid.

5 3. Two evolutionary processes P_1 and P_2 can be summed if and only if on a shared interval of the base helicoid P_1 followed by P_2 is identical to P_2 followed by P_1 . The sum of P_1 and P_2 is $P_1(t)[P_2(t)[v]]$, where t is a point in time and v is
10 a point in the volume domain of interest.

4. A fibre is a compact path-connected sub-volume. A fibre is associated to each base point. In other words the process time stamps every sub-volume that it affects.

15 5. A structure group is a 1-parameter subgroup of diffeomorphisms that define an evolution, e.g., vpmcf. Since the structure group consists of diffeomorphisms the process must be invertible. In particular, the process cannot induce
20 singularities in material space. It is preferable to support singularities, so we allow singularities to develop at the end of a process's time interval.

We emphasize that we seek only a geometrical
25 evolution - not necessarily the true physical evolution - that describes part of the structural framework. In the following example, we recognize uniformly expanding mean curvature flow creates the shape of the individual layers. Each discontinuity in the sediment terminates the
30 current flow model and is part of the initial conditions that define the new flow. The ensemble of flow problems describes the formation, but a more economical

representation can be defined if we can treat the entire set of restricted flow problems as a single mean curvature flow problem where evolution continues beyond the intermediate singularities. We look for an evolution
 5 of the set of initial conditions for the individual flow problems, given just the oldest sediment as an initial condition.

We describe a sedimentary sequence as a 4D fibre
 10 bundle.

1. The base of the bundle is a finite length piecewise linear curve.

2. A fibre is an infinitesimal layer of
 15 sediment.

3. The bundle's structure group is a set of diffeomorphism groups such that each group defines an instance of uniformly expanding mean curvature flow. Each leg of the bundle base defines a separate
 20 mean curvature flow problem. The transition between mcf problems is exactly matched by the discontinuity in the sediment.

Figure 3 shows an example of a 4D representation of
 25 a field in Turkmanistan. Each layer is a distinct mean curvature flow where the discontinuity is a curvature flow terminator. Working backwards from a flow termination, we see that it is much easier to identify the flow components in the image. Each flow component is
 30 a uniformly expanding set of solutions to mean curvature flow (or volume-preserving mean curvature flow). Ecker shows in his lecture notes that mean curvature flow can evolve cracks and holes in a smooth background. See, K.

Ecker, Lectures on Regularity for Mean Curvature Flow,
http://web.mathematik.unifreiburg.de/mi/analysis/lehre/WS0001/Ecker_WS0001.ps.

Therefore its usefulness is not limited to modeling
 5 smooth elastic behavior.

According to the invention, we show how to construct
 a meandering river as a fibre bundle. Figure 4 is an
 image of the MacKenzie River Delta.

In Figure 4, the river does not intersect itself,
 10 i.e., no oxbow structures are evident. Also, the river
 appears to have constant width. The structure as a fibre
 bundle is clear.

1. The bundle base is a line segment.
- 15 2. The fibre is any convenient approximation
 of the river channel in cross section, e.g., a
 trapezoid.
3. The structure group is the extended
 Euclidean group, which consists of rigid body motion
 20 plus scaling.

At each point along the channel we measure the cross
 section and record its position relative to the image
 coordinate axes whose origin is the lower left corner of
 25 the picture. Given the previous position of the cross
 section, we compute the update to the (x,y) plane
 rotation and translation.

We turn now to the question of recognizing the
 elementary shape basis elements in an implicit surface
 30 representation. Recall that we represent an implicit
 surface as the zero level set of the signed distance
 function (sdf). Our constructor solves the signed

distance function on a 3D structured grid with tri-linear interpolation as a local approximation to sdf.

By definition tri-linear interpolation $T(x,y,z)$ on a grid cell is

5

$$T(x,y,z) = A_0 + A_1x + A_2y + A_3z + A_4xy + A_5yz + A_6xz + A_7xyz.$$

where the coefficients $\{A_k\}$ are defined on the grid cell corners.

10

Each term in $T(x,y,z)$ is an independent 3D spherical harmonic polynomial in Cartesian coordinates. For convenience we enumerate these spherical harmonic

polynomials, using the classical Y_{mm} notation. (See R.

15

Baerheim, Coordinate Free Representation of the Hierarchically Symmetric Tensor of Rank 4 in Determination of Symmetry, Ph.D. thesis, University of Utrecht, #159, 1998, Appendix, pg. 141-143).

$Y(m,n)$	Monomial
$Y(0,0)$	1
$Y(0,1)$	z
$\text{Real}(Y(1,1))$	x
$\text{Imag}(Y(1,1))$	y
$\text{Real}(Y(2,1))$	xz
$\text{Imag}(Y(2,1))$	yz
$\text{Imag}(Y(2,2))$	xy
$\text{Imag}(Y(3,2))$	xyz

20

Here are the associated symmetry transformations and the corresponding isomorphism groups involving these spherical harmonic polynomials.

Term	Symmetry generators	Symmetry group
Constant	Constant	SO(3)
x	$[x] \sim [x]$	SO(2)
y	$[y] \sim [y]$	SO(2)

Z	$[z] \sim [z]$	SO(2)
X + Y	$[x, y] \sim [y, x]$	Z/2Z
X + Y + XY		
Y + Z	$[y, z] \sim [z, y]$	Z/2Z
Y + Z + YZ		
X + Z	$[x, z] \sim [z, x]$	Z/2Z
X + Z + XZ		
X + Y + Z	$[x, y, z] \sim [y, z, x]$ $[x, y] \sim [y, x]$	Tetrahedron group of order 12
XYZ	$[x, y, z] \sim [y, z, x]$ $[y, z] \sim [-y, -z]$ $[x, y] \sim [y, x]$	Symmetric(4)
XY	$[x, y] \sim [-x, -y]$	Z/2Z \oplus Z/2Z
	$[x, y] \sim [y, x]$	
YZ	$[y, z] \sim [-y, -z]$	
	$[y, z] \sim [z, y]$	
XZ	$[x, z] \sim [-x, -z]$	
	$[x, z] \sim [z, x]$	
XY + XZ	$[x, y, z] \sim [-x, -y, -z]$ $[y, z] \sim [z, y]$	Z/2Z \oplus Z/2Z
XZ + YZ	$[x, y, z] \sim [-x, -y, -z]$ $[x, y] \sim [y, x]$	
XY + YZ	$[x, y, z] \sim [-x, -y, -z]$ $[x, z] \sim [z, x]$	
XY + YZ + ZX	$[x, y, z] \sim [-x, -y, -z]$ $[x, y, z] \sim [y, z, x]$ $[x, y] \sim [y, x]$	Symmetric(4)

Symmetry analysis is a form of spectral analysis applied to the discrete spectrum that is associated with spherical harmonic polynomial expansions. Our estimates
5 of tri-linear interpolation coefficients are noisy, so we need a threshold for dismissing spectral lines.

Figure 5 shows some combinations of involved spherical harmonic polynomials, presented in spherical polar coordinates.

We are interested in conic section fibre bundle shapes. Here is the correspondence of shape to symmetry group.

Symmetry group	Candidate shapes
SO(3)	Sphere
O(2)	Cylinder, spherical torus, elliptical torus, hyperboloid
SO(2)	Cone, paraboloid
Symmetric(4)	Cube
Dihedral(4)	Ellipsoid
Dihedral(3)	Triangular prism
$Z_2 \oplus Z_2$	Rectangular prism
Z_2	Cyclide
{1}	Noisy data

5

According to the invention, mean curvature flow and volume-preserving mean curvature flow will now be discussed in further detail. We define a few terms that appear frequently herein. Given a 2D manifold M and a point $p \in M$, let $\{p_1, p_2\}$ be a local coordinate system for a region containing p and let n be an outward pointing normal at p . Finally the Euclidean inner product of vector U_i and V_j is denoted by $\langle U_i, V_j \rangle$.

Definitions

The First Fundamental Form (1st FF) is $g_{ij} = \left\langle \frac{\partial M}{\partial p^i}, \frac{\partial M}{\partial p^j} \right\rangle$.

15 The inverse of the 1st FF is denoted by g^{ij} .

The Second Fundamental Form (2nd FF) is $A = [h_{ij}] = - \left\langle \frac{\partial^2 M}{\partial^2 p^i p^j}, n \right\rangle$.

The Weingarten map is $W_i^j = g^{jk} h_{ki}$. (Einstein notation used.)

The eigenvalues of the Weingarten map are the principal curvatures. The trace of the map is the mean curvature, the determinant of the map is the Gaussian curvature. The norm of the 2nd FF $|A|^2$ is defined as the sum of the squares of the principal curvatures.

20

We define mean curvature flow and volume-preserving mean curvature flow.

Notation

5

(M_t) is a family of evolving smooth 2D manifolds such that $M = M_0$ is given.

$N(x, t)$ is the normal at $x \in M_t$.

$H(x, t)$ is the mean curvature evaluated at $x \in M_t$.

10

$h(t)$ is the average value of $H(x, t)$ on M_t .

Mean curvature flow (mcf) is defined as the solution to the initial and boundary value problem

$$\frac{\partial M_t}{\partial t} = -H(x, t) \cdot N(x, t). \quad [4]$$

15

Volume-preserving mean curvature flow (vp-mcf) is defined as the solution to the initial and boundary value problem $\frac{\partial M_t}{\partial t} = -(H(x, t) - h(t)) \cdot N(x, t)$. [5]

Figure 6 illustrates that, except in ideal circumstances (when the input is a smooth closed convex region or a graph), a surface evolves under mcf to a point. Technically, mcf develops a singularity in finite time. See, K. Museth, D. Breen, R. Whitaker, A. Barr, Level Set Surface Editing Operators, SIGGRAPH 2002.

25

A straightforward way to prevent annihilation of this shape is to stop the mcf after some number of time steps, inspect the results, and maybe resume the process. This is not convenient in a production environment. In fact, the manner in which uncontrolled mcf annihilates a shape enables us to attach a recognition procedure that mcf can call to decide when to ask the human for permission to resume the figure's evolution.

30

Figures 7a-f forms a series of six images showing vpmcf suppressing noise. See, A. Kuprat, A. Khamayseh, D. George, L. Larkey, Volume Conserving for Piecewise Linear Curves, Surfaces, and Triple Lines, Journal of Computational Physics, 172 (2001), pg. 98-118. In Figure 7a, the southern hemisphere is corrupted with a significant amount of Gaussian noise. By Figure 7c, it makes sense to consider how much additional noise, if any, must be removed before the smoothed result is an acceptable approximation.

We are interested in surfaces of revolution. The following result has been obtained regarding the behaviour of surfaces of rotation under vpmcf. See, M. Athanassenas, Volume-preserving mean curvature flow of rotationally symmetric surfaces, Comment. Math. Helv. 72(1997), pg. 52-66.

Theorem (Athanassenas)

Let M_0 be a smooth rotationally symmetric surface enclosing a sub-volume V . Let S be a slab of thickness $\tau > 0$ that is bounded by the $z = 0$ and $z = \tau$ height field planes. Suppose that M_0 satisfies the following two conditions.

- a. M_0 has a line of intersection in the $z = 0$ and $z = \tau$ height field planes.
- b. The end points of each line of intersection between M_0 and S meet an end of M_0 at a right angle.

If the volume of V is greater than τ times the area of M , then M_t evolves under vpmcf to a cylinder.

As an example of the condition on the lower bound on volume, consider the case of a right cylinder of height τ and radius r . This cylinder has volume V equal to $\pi r^2 \tau$, while its surface area M is equal to $2\pi r \tau$. Hence the lower bound on the volume is satisfied exactly when $\pi r^2 \tau \geq 2\pi r \tau^2$, i.e., $r \geq 2\tau$. Heuristically, the bound is satisfied for "squat" cylinders. We observe that a sphere cannot satisfy the volume to area relationship. To do so would imply that there exists $r > 0$ such that $\frac{4}{3}\pi r^3 / 4\pi r^2 = \frac{r}{3} \geq 2r$.

Figure 8 illustrates the orthogonality condition of the theorem proposed by Athanassenas. In this diagram we show two vertical cross-sections. In the figure on the left the intersection of the figure with the top and bottom planes must satisfy the right angle hypothesis. The curvature flow takes care of the irregular vertical surfaces either end of the figure. In finite time $vpmcf$ generates from the figure on the left the figure on the right.

Volume preservation is essential for earth model applications, so we prefer $vpmcf$ to ordinary mcf . Later in the description, we will use this theorem to reduce the discrepancy between an idealized representation of shape and a sampled data surface.

Another important class of smooth surfaces are those that are star-shaped. A surface is star-shaped if there exists a point P on the surface such that a line segment PQ that is entirely contained in the surface can join every other point Q in the surface.

It has been shown that star-shaped closed smooth surfaces are stable under mcf . See, K. Smoczyk, Star-

shaped hypersurfaces and the mean curvature flow,

Manuscripta Math. 95 (1998), pg. 225-236.

We show now that vpmcf suppresses additive high frequency harmonics before decaying the underlying low frequency shape signal. Vpmcf enjoys the property that surface area is always decreasing in time.

$$\frac{d |M_t|}{dt} = - \int_M (H - h)^2 dg, \leq 0. \quad [6]$$

We frequently need to compute mean and Gaussian curvature for a single valued surface over a plane, i.e., a graph. Suppose that $S = S(x,y)$. Then the formulae for mean curvature H and Gaussian curvature K are as follows.

$$K = \frac{s_{xx}s_{yy} - s_{xy}^2}{(1 + s_x^2 + s_y^2)^2} \text{ and } H = \frac{1}{2} \frac{(1 + s_x^2)s_{yy} - 2s_x s_y s_{xy} + (1 + s_y^2)s_{xx}}{(\sqrt{1 + s_x^2 + s_y^2})^3} \quad [7]$$

We model a surface as a collection of patches, where each patch is taken from a surface of revolution, say $S = (\phi(v) \cos u, \phi(v) \sin u, \psi(v))$, such that $v \in (a,b)$, $u \in (0, 2\pi)$, and $\psi(v) \neq 0$. The formulae for mean curvature H and Gaussian curvature K for a surface of revolution is as follows.

$$K = -\frac{\phi''}{\phi} \text{ and } H = \frac{1}{2} \frac{-\psi' + \phi(\psi'\phi'' - \psi''\phi')}{\phi} \quad [8]$$

For the proofs, see, M. do Carmo, *Differential Geometry of Curves and Surfaces*, Prentice Hall, 1976, pages 162-163.

We need to understand how mcf behaves when applied to a noisy surface S , where S is either single valued over a plane or is a surface of revolution. The above

formulae imply that if S is an entire graph, then the harmonic number N scales the mean curvature. Similarly, if S is a surface of revolution, then N^2 scales the mean curvature. (Spherical harmonic polynomials have a cosine factor, so these estimates remain valid under the natural heat equation eigen-function expansion.) Consequently, the mean curvature integral involves a scale factor of either N^2 or N^4 . Therefore the rate of change of surface area becomes very negative as N increases. We conclude that vpmcf eliminates high frequency harmonics during the initial stages of the evolution ahead of low frequency harmonics that form the ideal shape. A maximum or minimum in the ideal shape will appear to move as vpmcf eliminates corrupting noise, but the critical point's location will stabilize as the noise disappears. Importantly, when a critical point's location stabilizes, it does not move later in the evolution unless vpmcf begins to decay the shape. We remark that mcf can be turned off locally by resetting the mean curvature to zero.

We turn now to the question of how to decide when noise suppression turns into shape decay. Refer again to Figures 7a-f, which show the smoothing of a noisy sphere under vpmcf. Athanassenas's theorem does not apply, since the sphere fails the volume bound assumption. However, it still makes sense to apply Kuprat et al.'s vpmcf procedure to the shape. When we do this we get Figures 7c-f.

It is reasonable to say that noise suppression reduces Figures 7a-b to Figures 7c-d. It is harder to say if image noise suppression or shape decay accounts for the transformation to Figures 7e-f. Therefore, we want

vpmcf to proceed without manual intervention to eliminate noise but to seek guidance when the flow causes the underlying shape to decay. Here is a way to monitor the elimination of noise and detect decay of the critical
 5 points in an underlying shape that relies on vpmcf.

1. Given a characteristic length, we embed a series of conical shapes in the surface. The base of the cone is either the outermost 1D boundary of the surface
 10 or it is an inflection point curve surrounding the patch that contains the maximum or minimum.
2. We recognize minima and maxima in its 2D enclosure using a standard nested bounding box algorithm. If the surface is implicit, then we can localize the
 15 region by testing the implicit surface's triangulated parent.
3. Use this 2D enclosure as the top of the (noisy) cone. Note that we cannot assume that each maximum or minimum is topologically isolated, e.g., a ridge
 20 might exist.
4. Apply any mean curvature flow procedure, e.g., D3b, to the surface and monitor the effect on the cone's slant height. Mean curvature flow theory says that the slant height decreases as the noise is removed
 25 (it becomes straighter). However, when the mean curvature flow begins to destroy the intrinsic shape of the surface in the vicinity of the cone, then the slant height will decrease beyond a threshold. Therefore, the test for adequate smoothing is to
 30 compare the ratio of slant height before smoothing to the result obtained after each iteration.

Figure 9 is an aerial image of part of Big Bend National Park, showing the approximation of a plateau to
 35 a characteristic length scale cone. It is difficult to precisely locate the maxima on the plateau, but it is

easy to enclose the region containing the maxima in a tight loop. It is unimportant that the cone does not have a circular cross section.

Figure 10 is a side view of a noise cone structure.

5 When monitoring noise suppression on the surface of a geobody, e.g., it is useful to have a noise-monitoring device for thin undulating cross section. We replace a torus by a cone. We use the cone to monitor shear stretching and erosion of an interface. A clear instance
10 of this phenomenon is Figure 7c.

According to the invention, mean curvature flow and framework I/O will now be discussed in further detail. Singularities mark an end to the smooth evolution of a
15 shape under mcf. A singularity is frequently easier to identify on an image than is the interface that corresponds to the precise start of the flow. The flow imposes a natural partition of the framework. Each region in the partition is a self-contained expression of mcf.
20 When we think about sending and receiving an update to a framework, we prefer to send and receive a mcf problem with boundary conditions rather than an opaque byte stream. We specify the solution form - whether the flow uniformly expands or contracts the solution or smoothes
25 the initial data -and provide beginning and end surface data. We describe the intermediate surfaces by recording the time states that correspond to the intermediate surfaces. We also send critical point data for each intermediate surface. Interested applications run the
30 vpmcf script and reconstruct the update locally. We trade fast CPU for less fast I/O.

Here are three illustrations of this idea. Figure 11 is a NASA satellite image of the Labrador Trough. In this image we notice that the sediment resembles a longitudinal cross section of a brain with an attached spinal cord. Singularities separate "brain tissue" from the stem of the "spinal cord". A singularity also subdivides the "cerebellum".

Figure 12 shows a sequence of folded sediment on the coast of the Gulf of Oman. We model this as a uniformly expanding (seen right to left) solution to mcf. Ecker proved that a uniformly expanding solution to mcf is given by the equation $M_t = \sqrt{t} \cdot M_1$, provided that the initial fold is approximately a cone.

Figure 13 is an image illustrating progressive flattening of an overburden covering a large salt intrusion. We notice that the fault block that occupies the left half of the image (indicated by the lower white arrow) displays a gradual flattening in space and time as the top of the salt's intrusion is progressively reduced as the sediment was deposited on top of the salt (indicated by the upper white arrow).

According to the invention, a preferred technique of 2D parameterization will now be discussed in further detail. Many surface editing operations are more efficient when the operator can access the surface's parameterisation. Height field data uses the (x,y) co-ordinate plane as the parameter space and coordinate projection as the parameter space mapping. We explain how to obtain a parameterisation of a smooth surface S with no assumptions regarding the orientation of the surface relative to the (x,y) co-ordinate plane.

We claim that there exists an invertible projection of S onto a cylinder that has 0, 1, or 2 end caps.

1. Given any two closed curves C_1 and C_2 on S . We partially order the two curves, say $C_1 \leq C_2$, if
 5 there exists a 2D region R_2 on S such that $\partial R_2 = C_2$ and $C_1 \subseteq R_2$. We call the 2D region of S that is contained between $C_2 \setminus C_1$ the collar that is bounded by C_2 and C_1 .

2. From the classification of smooth surfaces
 10 in R^3 we know that S has Euler Characteristic $\chi(S)$ equal to 0, 1, or 2. The Euler Poincare Theorem says that $\chi(S) = \#(\text{maxima}) + \#(\text{minima}) - \#(\text{saddle points})$. Note that we use height as our Morse function, so the term "critical point" is a
 15 contraction for "height field critical point".

3. We will prove our claim by induction on the number of saddle points on S .

4. Suppose that the number of saddle points on S is zero.

20 a. If $\chi(S) = 2$, then Reeb's Theorem says that S is diffeomorphic to a round sphere, which is diffeomorphic to a cylinder with two end caps.

b. If $\chi(S) = 0$, then S must be
 25 diffeomorphic to a plane which is diffeomorphic to a cylinder with one end cap.

c. If $\chi(S) = 1$ then S has either 1 maximum or 1 minimum but not both.

d. Construct a 1st order Taylor series
 30 with center equal to the critical point and quadratic order error term.

e. Notice that the gradient term is trivial, since we expand about a minimum or maximum.

f. We apply a translation to the surface so that expansion point is the origin and has height equal to 0.

g. We conclude that after a suitable translation and (x,y) plane rotation a 2 term Taylor expansion about the critical point with a quadratic error estimator simplifies to a pure quadratic term.

h. Given $\varepsilon > 0$, we fit the Taylor expansion such that the error estimate is less than ε .

i. Then the Taylor series expansion within C_0 is a cap/cup. We know that a cap/cup is diffeomorphic to a plane and that a plane is diffeomorphic to cylinder with one end cap. Furthermore, the open end of the cylinder has boundary C_0 .

5. Suppose that the number of saddle points on S equals 1.

a. If $\chi(S) = 2$, then S possesses either (i) 2 maxima and 1 minimum or (ii) 2 minima and 1 maximum or (iii) 3 maxima or (iv) 3 minima.

b. Case (iii) is impossible, because Morse Theory says that a maximum contributes a 2D cell to the shape. If case (iii) were true, then

c. Case (iv) is impossible, because Morse Theory says that a minimum contributes a 0D cell to the shape. If case (iv) were true, then S contains no 2D cells.

Figure 14 is a diagram illustrating the Morse theoretical cell decomposition for a simple configuration of a capped and bent cylinder.

Morse Theory explains the cell decomposition of the shape. (See M. Hirsch, *Differential Topology*, Springer Verlag, 1976, pg. 156-164.)

5 d. This shape has a saddle point at location C.

 i. Morse Theory says that the surface contains a 1D cell that is attached to location C.

10 ii. We observe that this 1D cell is not a loop. Specifically, the point at location D is not part of the 1D cell.

15 e. This shape has a minimum at location D.

 i. Morse Theory says that the shape contains a 0D cell that is attached to location D.

20 f. This shape contains two maxima at locations A and B.

 i. Morse Theory says that the shape contains two 2D cells, and that each 2D cell is attached to a maximum.

25 ii. The boundary between the two 2D cells is the union of the 0D cell that is attached to location D and the 1D cell that is attached to location C.

30 iii. We decompose each 2D cell into the union of a Taylor series cap expanded about the maximum and a collar that is bounded by the loop suspended between locations C and D and the Taylor series circle of convergence.

35 g. Suppose that $\chi(S) = 1$. The Euler-Poincare formula says that the surface contains

either (i) 1 maximum and 1 minimum or (ii) 2 maxima or (iii) 2 minima.

i. An example configuration for case (i) is the upper half of a torus.

ii. An example configuration for case (ii) is a flat surface with two hills.

iii. An example configuration for case (iii) is a flat surface with two valleys.

h. Finally suppose that $\chi(S) = 0$. Then S contains either 1 minimum or 1 maximum, but not both. An example of this configuration is a single mountain or sinkhole attached to a plane.

6. We have specified the parametric mapping when S contains either 0 or 1 saddle point.

7. Now suppose that S contains $N-1$ saddle points. Choose any saddle point and pass a height field plane through it, subdividing S in two. At least one of the two parts contains fewer saddle points than does S . Define S^* to be this part of S .

a. By induction we know that S^* is diffeomorphic to either a cylinder with a hole in its lateral surface, or a cylinder that has 0 or 1 end caps.

b. Closing the hole in S^* corresponds to either closing a hole in the walls of a cylinder or to attaching an end cap to the cylindrical surface that we created in xyz space.

Figures 15-17 show diagrams to aid in the understanding of the bulls eye construction. In Figure

16, we invertibly map the possibly patched A to the planar unfolding of its interior faceted cylinder. Figures 17a and 17b illustrates how to perform the bulls eye construction in the region of a saddle point. The
 5 saddle point is indicated with the dot 10 in Figures 17a and 17b. This process is preferably repeated for every saddle point of the shape.

According to the invention, tri-linear
 10 interpolation, implicit surfaces, and critical points will now be described in further detail. In particular we herein discuss the analysis of the tri-linear interpolation approximation to the signed distance function on a 3D structured grid. We derive necessary two
 15 conditions that the tri-linear interpolator must satisfy if the grid cell contains a height field critical point. One condition specifies a relationship between the tri-linear coefficients and the critical value. The other condition establishes a second relationship among four of
 20 the tri-linear coefficients. Taken together, we show that a height field critical point for an implicit surface must be embedded in the grid cell faces and can never be found in the interior of the grid cell unless the implicit surface is a plane.

25 Let G denote a 3D structured grid with typical grid cell C . We assume that an implicit surface S is contained in G and in particular that $C \cap S \neq \emptyset$. We denote the tri-linear interpolation function on C by σ and we assume that C is small enough that σ is a good approximation to
 30 the signed distance function that implicitly defined S .

We begin with the definition of tri-linear interpolation

$$\sigma(x, y, z) = A(x, y) + B(x, y) \cdot z \quad (1)$$

5

where

$$\begin{aligned} A(x, y) &= a_0 + a_1x + a_2y + a_3xy \\ B(x, y) &= b_0 + b_1x + b_2y + b_3xy. \end{aligned} \quad (2)$$

10

For later reference, we note that A and B are harmonic, i.e.,

$$\nabla^2 A = \nabla^2 B = 0 \quad (3)$$

15

We are interested in the zeroth level of σ . If $\sigma = 0$, then either $B = 0$ or $B \neq 0$. We suppose that $B \neq 0$. Then

$$z = -\frac{A(x, y)}{B(x, y)}. \quad (4)$$

20

We know that height field critical points are found when

$$\frac{\partial z}{\partial x} = \frac{\partial z}{\partial y} = 0. \quad (5)$$

25

This condition is satisfied when

$$B \frac{\partial A}{\partial x} - A \frac{\partial B}{\partial x} = 0 \quad (6)$$

30

$$B \frac{\partial A}{\partial y} - A \frac{\partial B}{\partial y} = 0$$

Rewriting (6)

$$\frac{A}{B} = \frac{\frac{\partial A}{\partial x}}{\frac{\partial B}{\partial x}} = \frac{\frac{\partial A}{\partial y}}{\frac{\partial B}{\partial y}} \quad (7)$$

5 Using (7)

$$\begin{aligned} \frac{\partial}{\partial y} \left(B \frac{\partial A}{\partial x} - A \frac{\partial B}{\partial x} \right) &= \\ \left(\frac{\partial B}{\partial y} \cdot \frac{\partial A}{\partial x} - \frac{\partial B}{\partial x} \cdot \frac{\partial A}{\partial y} \right) + (B a_3 - A b_3) &= \quad (8) \\ (B a_3 - A b_3) &= 0. \end{aligned}$$

The Hessian matrix of 2nd partial derivatives
10 evaluated at the critical point is

$$\begin{aligned} \frac{\partial^2 z}{\partial x^2} &= \frac{-2 B \frac{\partial B}{\partial x} \left(B \frac{\partial A}{\partial x} - A \frac{\partial B}{\partial x} \right)}{B^4} = 0 \\ \frac{\partial^2 z}{\partial y^2} &= \frac{-2 B \frac{\partial B}{\partial y} \left(B \frac{\partial A}{\partial y} - A \frac{\partial B}{\partial y} \right)}{B^4} = 0 \quad (9) \\ \frac{\partial^2 z}{\partial x \partial y} &= \frac{B \frac{\partial^2 A}{\partial x \partial y} - A \frac{\partial^2 B}{\partial x \partial y}}{B^4} = \frac{B a_3 - A b_3}{B^4} = 0. \end{aligned}$$

15

We conclude that the Hessian matrix of 2nd partial derivatives is identically zero. We are led to consider what kinds of shape have the property that in a local
20 neighborhood of a critical point the matrix of second partial derivatives is identically zero.

We have enough information to compute the Gaussian curvature of $z = z(x, y)$. Recall that for a graph $z = z(x, y)$ that its Gaussian curvature $K(x, y)$ is

$$K(x, y) = \frac{\frac{\partial^2 z}{\partial x^2} \cdot \frac{\partial^2 z}{\partial y^2} - \left(\frac{\partial^2 z}{\partial x \partial y}\right)^2}{\left(1 + \left(\frac{\partial z}{\partial x}\right)^2 + \left(\frac{\partial z}{\partial y}\right)^2\right)^2} \quad (10)$$

We notice that the signum of $K(x, y)$ depends only on its numerator. Substituting (3) into the numerator of (9), we discover that the numerator of $K(x, y)$ is

$$-\left(\frac{\partial^2 z}{\partial x \partial y}\right)^2 = -(B \cdot a_3 - A \cdot b_3) + \left(\frac{\partial A}{\partial y} \cdot \frac{\partial B}{\partial x} + \frac{\partial A}{\partial x} \cdot \frac{\partial B}{\partial y}\right) \quad (11)$$

Hence the Gaussian curvature $K(x, y) \leq 0$ everywhere.

As an illustration we consider the "monkey saddle" $M(x, y)$, which coincidentally is also a spherical harmonic polynomial $M(x, y) = \text{Re}(Y_{33}) = .x^3 - 3xy^2$. The monkey saddle has a single critical point, which is the origin $(0, 0)$.

The matrix D of 2nd partial derivatives is

$$D = \begin{bmatrix} 6x & -6y \\ -6y & -6x \end{bmatrix}. \quad (12)$$

Substituting $(x, y) = (0, 0)$, we find that the 2nd partial derivatives matrix is identically 0. We conclude that the origin is a degenerate saddle point for $M(x, y)$.

Figure 18 shows two views of an example of a monkey saddle. In particular the monkey saddle is $M(x, y)$ given by the equation above. The image on the left is shaded according to mean curvature, while the image on the right is shaded according to Gaussian curvature. We have placed a white dotted circle around the critical point.

The critical point is a degenerate saddle point. We see this by substituting the samples defined by the white circle and observing the pattern of $+/-$ signs. As an example, let $0 < a < b$. Then $((+/-)a, (+/-)b)$ produces the

pattern $(-, -)$, $(-, +)$, $(-, -)$, and $(-, +)$ clockwise from Quadrant I.

The Gaussian curvature of the monkey saddle is (Gray, pages 382-383)

5

$$K(x, y) = -\frac{36(x^2 + y^2)}{(1 + 9x^4 + 18x^2y^2 + 9y^4)^2} \quad (13)$$

(See, A. Gray, *Modern Differential Geometry of Curves and Surfaces with Mathematica 2nd Edition*, CRC Press, 1998, pages 382-383).

Summarizing the analysis for $B \neq 0$, we have shown the following.

1. A grid cell contains at most one height field critical point.
2. If a grid cell does contain a critical point, then the critical point's coordinates are uniquely determined from the tri-linear interpolator's coefficients. We use this as a quick test for assessing the existence of a critical point in a grid cell.
3. The matrix of 2nd partial derivatives is identically zero when evaluated at the critical point.
4. The Gaussian curvature $K(x, y) \leq 0$ and equals zero exactly at the critical point.
5. $z = z(x, y)$ is harmonic, so by the Maximum Principle for harmonic functions on compact sets, we know that the minimum and maximum value for z on a grid cell will be found on the grid cell corners.

It has been remarked that the behavior of the tri-linear interpolation function is determined in the region

5 of a critical point by the behavior of $\frac{\partial z}{\partial x}, \frac{\partial z}{\partial y},$ and $\frac{\partial z}{\partial z}$. See,

G. Weber, G. Scheuermann, H. Hagen, B. Hamann, Exploring Scalar Fields Using Critical Isovalues, <http://graphics.cs.ucdavis.edu/~hamann/WeberScheuermannHagenHamann2002.pdf> ("Weber"). We agree, which is Morse Theory

10 should be applied.

Weber shows that a tri-linear interpolation function can have a critical point on the edge of a grid cell if and only if the tri-linear interpolation function is constant along the edge. Weber does not assume that the

15 tri-linear interpolation approximates a signed distance function. Weber also obtains a simple test for the existence of a maximum at grid cell vertex $(0,0,0)$ by looking at the value of the function at the tetrahedral corners $(1,0,0)$, $(0,1,0)$, and $(0,0,1)$.

20 In our situation Weber's condition says that $a_0 > \max(a_1, a_2, b_0)$ implies that $(0,0,0)$ is a maximum of $T(x,y,z) = A(x,y) + B(x,y)*z$. We note that $T(0,0,0) = a_0$ and that

$$\begin{aligned} \left. \frac{\partial T}{\partial x} \right|_{(0,0,0)} &= 0 \\ \left. \frac{\partial T}{\partial y} \right|_{(0,0,0)} &= 0 \\ \left. \frac{\partial T}{\partial z} \right|_{(0,0,0)} &= B(0,0) = b_0 \end{aligned} \tag{14}$$

25

Checking 2nd mixed partials

$$\frac{\partial^2 T}{\partial x^2} = \frac{\partial^2 A}{\partial x^2} + z \cdot \frac{\partial^2 B}{\partial x^2} = 0$$

$$\frac{\partial^2 T}{\partial y^2} = \frac{\partial^2 A}{\partial y^2} + z \cdot \frac{\partial^2 B}{\partial y^2} = 0$$

$$\frac{\partial^2 T}{\partial z^2} = 0$$

$$\frac{\partial^2 T}{\partial x \partial y} = \frac{\partial^2 A}{\partial x \partial y} + z \cdot \frac{\partial^2 B}{\partial x \partial y} = a_3$$

$$\frac{\partial^2 T}{\partial x \partial z} = \frac{\partial B}{\partial x} = b_1 + b_3 y \quad (15)$$

$$\frac{\partial^2 T}{\partial y \partial z} = \frac{\partial B}{\partial y} = b_2 + b_3 x$$

5

Therefore the first order Taylor series expansion of the tri-linear interpolation function about $(0,0,0)$ inside a grid cell cube is given by the expression

$$\begin{aligned} T(x, y, z) &= a_0 + b_0 z + (b_1 + b_3 y)xz + (b_2 + b_3 x)yz \\ &= a_0 + b_0 z + b_1 xz + b_2 yz + b_3 xyz + b_3 xyz \quad (16) \\ &= a_0 + B(x, y)z + b_3 xyz \end{aligned}$$

10

This says that in a local neighborhood of $(0,0,0)$ that the tri-linear interpolation function is a harmonic polynomial and therefore the Maximum Principle applies.

15

We conclude that on the tetrahedron formed by the four grid cell vertices that maximum occurs at the grid cell vertex a_0 or b_0 . We invoke Weber's assumption and conclude that the maximum occurs at a_0 . It is not necessary to assume the other inequalities in Weber's assumption.

20.

We consider now the case that $\sigma = 0$ and $B = 0$. We begin by observing that $\sigma = 0$ implies that $B = 0$ if and only if $A = 0$. Therefore,

$$y = -\frac{a_0 + a_1x}{a_2 + a_3x} = -\frac{b_0 + b_1x}{b_2 + b_3x}. \quad (17)$$

Again we look for solutions to the zero gradient equation.

5

$$\frac{dy}{dx} = -\frac{a_1a_2 - a_0a_3}{(a_2 + a_3x)^2} = 0 \text{ implies that } a_1a_2 - a_0a_3 = 0$$

and

$$\frac{dy}{dx} = -\frac{b_1b_2 - b_0b_3}{(b_2 + b_3x)^2} = 0 \text{ implies that } b_1b_2 - b_0b_3 = 0 \quad (18)$$

Again we obtain a relationship among the tri-linear interpolator coefficients that must be satisfied in order that a grid cell face contain a critical point on a curve running through the grid cell face.

Suppose that a grid cell face contains a critical point of a curve. Again the second derivative $\frac{d^2y}{dx^2} = 0$, so we characterize the nature of the critical point by sampling the gradient on a tight neighborhood of the critical point.

We conclude that there exists at most 1 critical point on a curve running through a grid cell face and that the (x, y) coordinates of a critical point are uniquely determined in terms of the tri-linear interpolator's coefficients.

According to the invention shape index and shape identification techniques will now be described in further detail. According to a preferred embodiment, shape identification depends on a dimension - independent

measure of the principal curvatures at a point known as the Koenderink and van Doorn shape index si .

$$si = \frac{2}{\pi} \arctan \frac{\kappa_1 + \kappa_2}{\kappa_1 - \kappa_2} = \frac{2}{\pi} \arctan \frac{H}{\sqrt{H^2 - K}},$$

where $\kappa_1 \geq \kappa_2$.

- 5 Shown below is a chart of the shape index map's range $[-1.0, +1.0]$, which goes from most concave to most convex. We note that a shape index value of zero corresponds to a zero mean curvature surface, which for the case of a compact surface, equates to a catenoid or a
- 10 compact planar region.

Local shape	si interval	Local shape	si interval
spherical cup	$[-1, -7/8)$	saddle ridge	$[1/8, 3/8)$
trough	$[-7/8, -5/8)$	ridge	$[3/8, 5/8)$
rut	$[-5/8, -3/8)$	dome	$[5/8, 7/8)$
saddle rut	$[-3/8, -1/8)$	spherical cap	$[7/8, 1]$
saddle	$[-1/8, 1/8)$		

- Cantzler et al. have computed a correspondence between shape attributes defined by a Gaussian and mean
- 15 curvature value pair and the shape index map range. See, H. Cantzler, R. Fisher, Comparison of HK and SC curvature description methods, <http://www.dai.ed.ac.uk/homes/rbf/hc3dim.ps.gz>. See, the following tables.

	K < 0	K = 0	K > 0	Shape	Index range
H < 0	Saddle Valley (Sv Hy)	Concave Cylinder (-Cy)	Concave Ellipsoid (-El)	Concave Ellipsoid (-El)	$S \in [-1, -5/8)$
H = 0	Minimal (M Hy)	Plane (Pl)	Impossible	Concave Cylinder (-Cy)	$S \in [-5/8, -3/8)$
				Hyperboloid (Hy)	$S \in [-3/8, 3/8)$
				Convex Cylinder (+Cy)	$S \in [3/8, 5/8)$
H > 0	Saddle Ridge (Sr Hy)	Convex Cylinder (+Cy)	Convex Ellipsoid (+El)	Convex Ellipsoid (+El)	$S \in [5/8, 1]$

As an example, we compute the shape index of a torus.

5

a. The torus's parameterization is

$$((a+b \cdot \cos v) \cos u, (a+b \cdot \cos v) \sin u, b \cdot \sin v),$$

where we assume that $a > b > 0$.

b. The principal curvatures are $k_1 = -\frac{\cos v}{a+b \cdot \cos v}$ and $k_2 = -\frac{1}{b}$.

10 c. Therefore $\frac{k_1 + k_2}{k_1 - k_2} = -(1 + \frac{2b}{a} \cos v)$.

d. This quotient covers the range $[-3.0, +1.0]$; hence the shape index covers the interval $[-0.80, +0.50]$, which corresponds to "trough" to "ridge".

15 Certain principal curvature pairs are distinguished.

1. If $\kappa_2 = \kappa_1$, then the shape index is ± 1.0 , as the $\text{signum}(\kappa_2) = -/+1$.

2. If $0 = \kappa_2 > \kappa_1$, then the shape index is $-1/2$.

20 3. If $\kappa_2 > \kappa_1 = 0$, then the shape index is $1/2$.

4. If $\kappa_2 = -\kappa_1$, then the shape index is 0.

5. The shape index of a maximum is 1.0.

6. The shape index of a minimum is -1.0.

25 7. If the shape index is discretized in increments of size Δs , then the principal curvatures will

be discretized according to the following formulae

Shape index expresses a relationship between
 5 principal curvatures. For example, we expect the shape index in the region of an inflection point is approximately 1/8. Plugging into the shape index definition, we discover that

$$10 \quad \kappa_2 = \kappa_1 \cdot \left(\frac{\tan\left(\frac{\pi}{2} \cdot \frac{1}{8}\right) - 1}{\tan\left(\frac{\pi}{2} \cdot \frac{1}{8}\right) + 1} \right) = -0.99023 \cdot \kappa_1.$$

The shape index enables a human to express a threshold change in curvature in a dimension-independent manner. This correspondence is fundamental to the
 15 robustness of our shape identification scheme. Measurements are always tainted with noise. Therefore it is preferable to identify intervals rather than point values for attribute correspondence.

Definitions

Let $A, B \in S$ and let s_A, s_B be the shape index at A, B .

20 By definition $\tan\left(\frac{\pi}{2} \cdot s^A\right) = \theta^A$ and $\tan\left(\frac{\pi}{2} \cdot s^B\right) = \theta^B$, where

$$\theta^A = \frac{\kappa_1^A + \kappa_2^A}{\kappa_1^A - \kappa_2^A}, \text{ where } \kappa_1^A \text{ and } \kappa_2^A \text{ are principal curvatures at } A.$$

Likewise for θ^B .

$$\text{Thus } \tan\left(\frac{\pi}{2} \cdot (s^B - s^A)\right) = \frac{\theta^B - \theta^A}{1 - \theta^B \cdot \theta^A} \text{ or } (s^B - s^A) = \frac{2}{\pi} \arctan\left(\frac{\theta^B - \theta^A}{1 - \theta^B \cdot \theta^A}\right)$$

This formula relates the shape index principal curvature quotient in shape index increments. For example

$$\text{if } (s^B - s^A) = \frac{1}{8}, \text{ then } \tan\left(\frac{\pi}{16}\right) = 0.0034 = \frac{\theta^B - \theta^A}{1 - \theta^B \cdot \theta^A}.$$

Holding θ^A fixed, then $\tan\left(\frac{\pi}{16}\right) \cdot (1 - \theta^B \theta^A) = \theta^B - \theta^A$ implies that

$$\theta^B = \frac{\tan\left(\frac{\pi}{16}\right) + \theta^A}{1 + \tan\left(\frac{\pi}{16}\right) \cdot \theta^A} = \frac{0.0034 + \theta^A}{1 + 0.0034 \cdot \theta^A}.$$

Now we can utilize the formula relating the value of a shape index to the ratio of the constituent principal curvature.

According to a preferred embodiment of the invention, techniques for curvature-adaptive sampling of a smooth surface will now be described in further detail.

Due to popularity of 2D FFT methods, it is common practice to sample a surface based on a fixed spatial step size. For smooth data, we know that a low order Taylor polynomial expansion can supply sample data to whatever a priori precision and at whatever spacing is acceptable. There is no need to store a large array when an algebraic expression can be evaluated on demand. Our method for curvature-based sampling is straightforward.

1. We are given a cloud of points. Using Hoppe's tangent plane fitting procedure (Hoppe, pages 22-25), we loop through the input point cloud fitting tangent planes.

2. At each tangent plane, we determine if the parent point is a height field critical point. We record the set of all critical points $\{C_k\}$. We use the symbol $T(C_k)$ to denote the tangent plane at C_k .
3. At each critical point C_k , we define a neighborhood $N(C_k)$ about C_k in the point cloud such that the tangent plane $T(C_k)$ is a parameterization of the triangulation of the points in $N(C_k)$. Abusing notation slightly, we use $N(C_k)$ to denote the triangulation of the point cloud.
4. Using equations (4.7₁) and (4.7₂) we estimate both principal curvatures and the associated shape index on $N(C_k)$.
5. Given a shape index increment, we apply the analysis developed in Section 8 to partition $N(C_k)$ into shape index equivalence classes. We chose to seed the shape index equivalence classes with critical points so that there is the least ambiguity in the shape index assignment.
6. If the critical point neighborhoods do not cover completely the implicit surface, then search the remaining surface for regular points that have an unambiguous shape index interval assignment.
7. Bin the remaining unassigned sample points to new shape index equivalence classes.
8. Assign each shape index equivalence class to a distinct grid cell.

9. Done.

This algorithm uses just curvature information, since we apply it to the unorganized input point cloud.

5 We can improve the $N(C_k)$ partition if we know a priori that the shape identification procedure described above has been applied. Using the information generated during shape identification, we construct a low order Taylor polynomial expansion that equals as a point set a shape index equivalence class. We begin with an estimate of the error that we expect if we expand the signed distance function (sdf) in a 1st order gradient Taylor expansion plus quadratic remainder term. Let $s(x, y)$ represent the sdf over an open neighborhood $N(x_0, y_0)$ in the (x, y) plane.

15 Then the Taylor expansion for s in $N(x_0, y_0)$ is

$$s(x, y) = s(x_0, y_0) + \left[\frac{\partial s}{\partial x}(x_0, y_0) \cdot (x - x_0) + \frac{\partial s}{\partial y}(x_0, y_0) \cdot (y - y_0) \right] + \frac{1}{2!} \left[\frac{\partial^2 s}{\partial x^2}(\alpha x, \alpha y) \cdot (x - x_0)^2 + \frac{\partial^2 s}{\partial x \partial y}(\alpha x, \alpha y) \cdot [(x - x_0)(y - y_0)] + \frac{\partial^2 s}{\partial y^2}(\alpha x, \alpha y) \cdot (y - y_0)^2 \right]; \alpha = \alpha(x, y) \text{ and } 0 < \alpha < 1.$$

We translate s in the z -direction so that $s(x_0, y_0) = 0$, eliminating the constant term. Now rotate the orthonormal basis defined by the tangent plane of the sdf at (x_0, y_0) plus the z -axis so that it coincides with the orthonormal basis formed the canonical co-ordinate system.

25

Notes:

- a. Rotation in the (x,y) coordinate plane will align any pair of orthogonal vectors the coordinate plane axes.
- b. Rotating the surface so that $s(x_0, y_0)$ is a maximum causes $\nabla s(x_0, y_0) = 0$.

Combining the translation and the rotation, the Taylor expansion is

$$s(x, y) = \frac{1}{2!} \left[\frac{\partial^2 s}{\partial x^2}(\alpha x, \alpha y) \cdot x^2 + \frac{\partial^2 s}{\partial y^2}(\alpha x, \alpha y) \cdot y^2 \right]; \quad 0 < \alpha < 1.$$

The coefficients inside the square brackets are the principal curvatures at $(\alpha x, \alpha y)$. They can be computed from the mean and Gaussian curvature at $(\alpha x, \alpha y)$.

$$H(\alpha x, \alpha y) = \frac{1}{2!} \left[\frac{\partial^2 s}{\partial x^2}(\alpha x, \alpha y) + \frac{\partial^2 s}{\partial y^2}(\alpha x, \alpha y) \right]$$

$$K(\alpha x, \alpha y) = \frac{\partial^2 s}{\partial x^2}(\alpha x, \alpha y) \cdot \frac{\partial^2 s}{\partial y^2}(\alpha x, \alpha y)$$

Using shape analysis, the true value of every term in the Taylor expansion is known. The Taylor disk records the first two terms in the expansion, the expansion point, the disk's radius of convergence, and the maximum error incurred on the convergence disk when a sample coordinate is approximated by just the constant and linear gradient terms. When an intersection curve is established, then the definition of the curve is attached. There is a separate attachment for every intersection curve.

The α parameter is interesting. Given the center of the Taylor disk, the disk radius, and polar angle increments then the α parameter describes the intersection as well as the principal curvatures along the intersection curve. (A more descriptive name for this parameter is "wireframe".) This parameter determines the adequacy of the interpolating function in the 3D grid. In other words, the adequacy depends on the curvature of the parent surfaces along the intersection path.

10 We prepare the topological analysis of a shape-based surface by creating a manifold whose charts are point sets that correspond to shape index intervals. We call this a shape index manifold. We explained above how to construct the manifold's charts and how to estimate the differential properties of a chart. These tasks make sense with no external context, i.e., a background framework. We refer to properties that make sense in this self-contained context as "intrinsic". Any property of a manifold that is not intrinsic is "extrinsic". An example of an extrinsic attribute is the relationship between the boundaries of a surface and the boundaries of a shape index manifold.

25 An intrinsic boundary is one that remains a boundary under rigid motion. It is a Cartesian tensor by virtue of this definition. This boundary separates regions that are well approximated by patches taken from a surface of revolution. An extrinsic boundary is a boundary that owes its existence to the configuration of background surfaces. Should the background surfaces move then the shape of the intersection and indeed the very existence of the intersection can change. The choice of solver depends on the dataset assumptions. The Shapes @ library

does not provide recognition or interaction services pertaining to intrinsic boundaries. We agree that a characteristic of a sound approach to point set classification is a robust algorithm to compute the intersection of two extrinsic boundaries. But we go one step further and say that intersection in a region that is devoid of extrinsic structure can be still be quite complicated, if the intersection involves a non-empty subset of a non-differentiable interface that separates two shapes.

We seek a data structure that conveys a framework overview. We want it to contain the complete boundary representation for the framework plus a synopsis of the shape of every framework surface and curve. We envision using this data structure to reply to browser level framework data base queries when the caller does not want to open the framework with the standard geometry services toolkit.

We define a structural synopsis to be a Shapes/GQI topology graph (also known as a boundary-representation or "b-rep") plus a shape index manifold description of every 2D node in the b-rep.

Preferably, a Reeb graph is used to describe a configuration's Morse critical points and homotopic skeleton. See, M. Hilaga, Y. Shinagawa, T. Komura, T. Kunii, Topology matching for full automatic similarity estimation of 3D, SIGGRAPH 2001, pg. 203-212, and Silvia Biasotti, Topological techniques for shape understanding, <http://www.cg.tuwien.ac.at/studentwork/CESCG-2001/SBiasotti/>. We recall the definition of a Reeb graph. Let M be a path-connected manifold and let f be a real-valued on M . Then the Reeb graph associated with $(M,$

f) is a set of $(M, f), R)$ equivalence classes that is defined by the relation $(x, f(x)) \sim (y, f(y))$ if and only if $f(x) = f(y)$ and x, y are members of $f^{-1}(f(x))$. In practice, the nodes and arcs in a Reeb graph are

5 determined from continuous sampling of homotopic identification of height field contours. Since the height field is a Morse function, we obtain information regarding each non-degenerate critical point and the cell

10 of 2D parameterization herein summarizes the relevant facts from Morse Theory.

Figure 19a shows the Reeb graph of a standard torus. Figure 19b schematically illustrates a 2D cell suspension that is induced from the axes and planes of symmetry and

15 critical point theory. The Reeb graph's nodes in this case are critical points on the torus, since the critical points are isolated and non-degenerate. The graph contains 4 nodes. The bottom and top nodes correspond to the height field minimum and maximum. These two points

20 lie on an isoparametric curve of constant positive Gaussian curvature. The other two nodes correspond to the lower and upper saddle points. They too lie on an isoparametric curve, but this curve has constant negative Gaussian curvature. It is easy to see that the symmetry

25 group of the torus leaves invariant the orbit of a saddle point as well as the orbit of the min/max. We remark that observing this invariant behavior is an easy way to discover symmetry transformations.

A Reeb graph describes homotopic equivalence. Reeb's

30 representation has no concept of shape. The Reeb graph says nothing about Gaussian curvature or mean curvature or shape index. There is no mention of the two opposing

curves of zero Gaussian curvature. Nor is there a description of the shape of the saddle point curve that bounds the interior void. Homotopic equivalence does not leave invariant 2D regions of constant shape index, so it is not possible to reason about symmetry orbits under Reeb equivalence.

Neither the Hilaga nor Biasotti references augment the Reeb graph substrate with curvature information, citing the natural instability of curvature estimation in noise. We agree that curvature estimation in a noisy environment is difficult, but we have above that it makes sense to treat a noisy surface as a smooth substrate that is contaminated with noise. We think of the representation of a noisy surface as a minimization problem in Lagrangian mechanics. The smooth approximant represents the kinetic energy in the decomposition. We define the curvature of the original surface to be that of the smoothed component of the original surface. The Riemann integral of the discrepancy between the smooth approximant and the original surface is a measure of the potential energy in the original surface. Noise introduces uncertainty into the curvature estimate. We compensate for this uncertainty by working with shape index intervals, rather than a point-specific value. We define a shape synopsis diagram (SSD) to a Shapes/GQI boundary representation where a 2D node is a shape index manifold.

We comment further that Hilaga reports the development of a similarity metric for a pair of triangulated surfaces S_1 and S_2 . Their idea is to create a level of detail hierarchy for each surface. The authors summarize each level of detail by constructing a Reeb

graph of the coarsened surface. Hilaga chooses the Reeb function to be the integral of geodesic distance measured at every vertex of S_1 and S_2 . Hilaga approximates the integral using Dijkstra's Algorithm. Hilaga argues that
5 this Reeb function is superior to a height field because the integral is insensitive to orientation.

We want to compare Hilaga's method to the method of the present invention. This is not easy. Hilaga works with triangulated surfaces rather than implicit surfaces.
10 Consequently we must be careful regarding the meaning of the term "geodesic path". On a smooth surface we can define a geodesic curve to be the straightest possible path or the shortest possible path, since the two characterizations coincide. On a triangulated surface
15 they do not. As is common practice, we select "straightest possible" geodesics because an existence proof is available for "straightest possible" whereas none exists if instead we opt for "shortest possible" geodesics.

20 We restrict attention to a single surface of revolution S , because there exists a theorem that says that a parallel on S is a geodesic exactly when the tangent vector at any point on the surface is parallel to S 's axis of symmetry. The symmetry group of S honors this
25 constraint, so the geodesic is an orbit under the action of the symmetry group.

Figure 20 is cross section of the torus shown in Figure 19a. Figure 20 shows the torus opened along a planar surface that joins the saddle point circular orbit
30 and the min/max circular orbit.

In Figure 20, we have overlaid the symmetry group orbits associated with critical points. We measure

criticality against the standard height field Morse function, because geological data is naturally observed in depth. We free ourselves of orientation and pose limitations by working with the symmetry group orbits of critical points rather than the isolated critical points themselves.

Figure 21 is a schematic of the shape synopsis diagram (SSD) of the torus shown in Figure 19a. The SSD reports locations in normal position coordinates and uses a homogeneous transformation to correctly position this data in model space. We also note that an SSD takes little storage beyond that already needed to instantiate the b-rep. We have placed details of the shape index manifold and shape index chart provided below.

Since an SSD augments the standard b-rep we attach a spatial frame to the b-rep node to reference the SSD. Since the top-level node in the SSD contains a database identifier, standard navigation methods can be used to locate the b-rep given the SSD. We call attention to the arrow notation in the SSD. We use an arrow to define the correspondence of 1D chart boundaries to 2D charts. The arrow that is attached to the concave chart signifies that the chart does not bound a sub-volume along its outside. Similar remarks pertain to the convex chart.

The Reeb graph of a cyclide is identical to the Reeb graph of a torus, as expected since the standard Reeb graph does not consider shape. The difference between a cyclide SSD and a torus SSD is the absence of circular orbits connecting critical points. That is, all of the height field critical points for a cyclide are isolated and are fixed by the cyclide's back to front reflection operator.

Figure 22 is a cyclide that is shaded according to Gaussian and mean curvature.

Next we construct the SSD for a 2-torus. Figure 23a is a bi-torus with its associated REEB diagram. Figure 23b is the visual representation of the bi-torus shape synopsis diagram. A shape index manifold is a patchwork, with each patch taken from a surface of revolution. So it makes sense to display the surfaces of revolution, where each surface is decorated with the bounding curves that define the patch selection. On the bi-torus's SSD there are two thin circular arcs plus the outer circle identify the two toroidal components in the bi-torus. We attached the "slab" label to the connective material between the two tori, because we perceive the top of the bi-torus to be flat, i.e., its Gaussian curvature is zero. The slab's internal boundary joins the upper and lower parabolic curves on both tori. We have suppressed the 1D orbits and critical point assignments to keep the diagram readable. The bi-torus is a genus 2 sphere, so there is 1 minimum and 1 maximum. Since the tori are tilted, the height field does not see the any critical points along either saddle point orbit. Finally, the interior surfaces of the slab are concave (hyperbolic) in order to conform to the torus's exterior convex surface.

The differences between an SSD and a Reeb graph are very clear. The use of homotopic identification means that the Reeb graph cannot distinguish homotopic figures that have significantly different curvature, e.g., a convex figure from a concave figure. Therefore shape index analysis is meaningless in the context of a Reeb graph. We conclude that although we can map a Reeb graph into an SSD, a Reeb graph cannot support a shape

index manifold.

According to a preferred embodiment of the invention, an efficient hierarchical surface

5 representation will now be described. We represent an implicit surface's signed distance function in a narrow band octree encoding of a regularly spaced Cartesian grid. We discuss herein how curvature and shape analysis of the implicit surface simplify the octree as a data
10 structure. Smoothing or editing in general is likely to change a prior shape analysis, so we will also describe herein an adjunct shape index representation that enables fast updating of the octree's information archive.

- 15 1. We begin by computing the shape index on the implicit surface at the finest resolution in the octree.
2. We partition the shape index data into equivalence classes.
- 20 a. We find the finest resolution octants that contain the surface's height field critical points.
- b. We define the following shape index relation on the octant corners that were located in the
25 previous step.
- c. We say that two octant corners are related when that their respective shape index values are contained in the same Cantzler sub division of the fundamental space $[-1.0, +1.0]$ and that
30 both values are bounded away from both ends of the Cantzler subdivision.
- d. We make a second pass over every equivalence class of octree nodes that contains less than a

threshold number of samples. Let v be such a node and suppose that v is on the frontier of shape index equivalence classes χ_1 and χ_2 .

e. If χ_1 and χ_2 are approximated by a single elementary shape instance, then we will assign the node v to either χ_1 or χ_2 .

f. If χ_1 and χ_2 are not approximated by a single elementary shape instance, then we assign v to χ_j if the error in the elementary shape approximation is less than a threshold

3. We introduce the shape index information to the coarser levels of the octree.

a. We say that a low-resolution octant is stable if there exists an elementary shape representation for all highest resolution level nodes that are controlled by the coarse level octant.

b. We record stability status. If a low-resolution node is stable, then it will use the elementary shape's algebraic evaluators for signed distance, mean and Gaussian curvature, etc.

c. We recognize that a stable low-resolution octree node v has the same shape resolution as v 's finest resolution level components. If we want a truly coarser approximation, then we develop a separate family of elementary shapes for each resolution level in the octree.

4. We prune the stable regions of the octree.

- a. Given an octant Q at level L such that its leaf level resolution is part of an ideal elementary shape.
- b. We set a status bit in Q that says it coarsely resolves part of an ideal shape.
- c. Prune the branch of the octree rooted at Q
- d. If Q does not coarsely resolve part of an ideal, then we keep the branch rooted at Q . Furthermore, we may need to use the leaf-level interpolator to estimate curvature.

The situation most favorable to this algorithm is when the root surface S^* contains a large stable region. This can happen if the leaf-level surface S contains a large region of zero Gaussian curvature, in which case the shape index for the region is $\frac{1}{2}$ or $-\frac{1}{2}$. Another favorable situation is that both the mean curvature and Gaussian curvature are constant, e.g., a sphere, so that the shape index is again a constant.

Figure 24 is a diagram of the octree with a coarse level and leaf level shape index relationship indicated. Consistent texture-coding between corresponding regions indicates a stable shape index region.

We consider two examples. The Figure 25 is a diagram shows part of the French model. A single octree leaf defines each plateau. The hemispherical depression has constant mean curvature and constant Gaussian curvature, so in both regions only one octree leaf is needed.

Figure 26 is an image of the topography of Crater Lake, Oregon. Figure 26 shows two large plateaus in the Southwest part of the lake basin. There are large flat regions of the lakebed, so this algorithm will represent these regions economically. The small elevation bumps on the lakebed will be enclosed in extruded cylinders.

We anticipate that the algorithm will perform well on the large trimmed conical plateau in the rear.

According to a preferred embodiment of the invention, an implicit surface shape identification technique will be described. In particular we show how to uniformly approximate an implicit surface by a patchwork of smooth shapes, where each shape is a section of a surface of revolution. The implicit surface is not required to be smooth. We say that the volume between the given implicit surface and the patchwork of smooth shapes measures the misfit of the approximation. We improve the uniform approximation by reducing the misfit. We reduce the misfit by approximating the volume as a Riemann sum of generalized prisms.

Shape identification provides a much higher density of information. Figure 27 shows a salt weld in the Gulf of Mexico. See, M. Hodgkins, M. O'Brien, Salt sill deformation and its implications for subsalt exploration, The Leading Edge, August 1994, pg. 849-851. We enumerate the shapes that collectively represent this complicated geobody.

The shape legend for this image is as follows.

1	Paraboloid cap	6	Toroidal sector
2	Cylinder	7	Barrel
3	Toroidal sector	8	Conical sector
4	Barrel	9	Toroidal sector
5	Conical sector	10	Cone

Now we specify the shape identification algorithm.

Notation

S A noisy implicit surface.

- S^* A smoothed version of S .
 G A 3D regularly spaced grid
 C A grid cell in G with corners $\{c_0 \dots c_7\}$.
 σ The signed distance function defined on C such
5 $\sigma^{-1}(0) = S \cap C \neq \emptyset$.
 τ Tri-linear interpolation associated with grid
cell C that approximates the signed distance
function σ on C .
 σ^* The symmetry group of σ .

10

Shape identification algorithm

1. We are given a 3D rectangular or rectilinear grid G that contains an implicit surface S .
- 15 2. Construct a smooth surface S^* from S , eliminating noise, but not low frequency intrinsic shape.
3. Sample S^* such that there exists a sample at each entry and exit point on each grid cell face in G . We know how to do this, since we know the nature of
20 a smooth shape that tri-linear interpolation can represent.
4. For each S^* sample point estimate the mean and Gaussian curvature.
5. Compute the shape index at every S^* sample point.
- 25 6. Mark those samples that are close to the center of a Cantzler shape index interval.
7. Mark those grid cell samples that are height field critical points, i.e., minima, maxima, and saddle points. (We know that these occur at grid cell
30 corners only.)

We identify shapes on S^* .

8. For each S^* critical point select grid cells
35 attached to the critical point that have consistent mean curvature, Gaussian curvature, and shape index

estimators at all sample points in the grid cell
 These grid cell sets define the initial equivalence
 classes.

9. We want to define a shape from the region of S^*
 inside the grid cell equivalence class. We check
 that each admitted grid cell's tri-linear
 interpolant has the same symmetry group. If there
 is no common symmetry group, then we subdivide the
 equivalence class into subclasses that do have a
 shared symmetry group.

10. Using the shape index data and the symmetry group,
 identify a surface of revolution that best fits the
 curvature and unit normal vector field data.

Let C be a grid cell that is unassigned to a grid
 cell equivalence class, but is adjacent to a grid cell
 that has been assigned to a grid cell equivalence class.
 We want a condition to test for admission to the
 equivalence class.

11. There are two categories of grid cells in an
 equivalence class. A member grid cell is either
 "shapely" or is a "misfit".
12. In order for the candidate grid cell to be admitted
 as "shapely", it must satisfy the following
 conditions.
 - a. Its tri-linear interpolation function has the
 same symmetry group as all other shapely grid
 cell members.
 - b. If a shapely grid cell in the equivalence class
 shares a grid cell face with the candidate grid
 cell, then they share a smooth boundary across
 the grid cell face.
 - c. We re-compute the shape parameter vector and
 re-test all grid cells in the equivalence
 class. No "misfit" grid cell is allowed to

exceed the misfit tolerance and no shapely grid cell can become a misfit.

13. Test if the candidate grid cell is shapely.

14. If not, then test if the candidate can be considered a "misfit".

a. A misfit must be less than some threshold and no point on the surface sample in the candidate grid cell can be further from the ideal shape than some other threshold.

15. If the misfit is acceptably small, then we mark the grid cell as a "misfit" and admit the grid cell.

We specify a misfit reduction algorithm later in this part of the description.

It may be that some grid cells have not been assigned to an equivalence class. These grid cells are not associated with a shape that has a critical point in the smoothed implicit surface S^* .

16. Form a new equivalence class by finding connected sets of grid cells where the individual grid cell tri-linear interpolation functions have the same symmetry group and whose shape index samples lie in the same Cantzler shape index interval.

It may be that some grid cells can be assigned to more than one equivalence class. If we have a choice, then we assign the candidate to the class that accepts the candidate as shapely.

It may be that some grid cells have not been unassigned to an existing equivalence class. Since S^* is smooth, we know that noise is not a contributing factor.

Instead, we have uncovered a set of grid cells that represent a rapid change in shape. When we encounter a grid cell of this type, then we deform the shape in the grid cell to conform to any adjacent grid cell and assign
5 it to the equivalence class that forces the least amount of deformation.

Two equivalence class shapes may fail to connect in a region where they should. When this happens, we deform the respective shape in those boundary grid cells until
10 they match the tri-linear interpolation function in each grid cell.

We now discuss the interface between two grid cell equivalence classes. If a grid cell face separates the two equivalence classes, then we call the interface
15 "sharp", otherwise the interface is "diffuse". If the interface is "sharp", then there exists a 1D boundary separating the two shapes. We compute this boundary by equating the two quadratic surface expressions and solving. This is not always smooth, so it will be
20 necessary to blend a narrow region on each side of the intersection curve. If the interface is diffuse, then we have a 2D region of overlap between the two shapes in which the smoothing can be naturally accommodated. We fit a shape to the overlap. We close this topic by checking
25 this analysis against two adjacent grid cells that have different conic section fibre bundle shape approximations. We conclude that the analysis is valid, since tri-linear interpolation is continuously differentiable on the grid cell face that separates the
30 two adjacent grid cells.

Now we overlay the patchwork shape on top of the original implicit surface S and look for chances to

reduce the misfit. We will do this by approximating the volume as a 3D Riemann integral. Our misfit reduction procedure is as follows.

5 Misfit reduction algorithm

1. We project the noisy implicit surface onto the patchwork smooth surface. We identify connected regions of the implicit surface that are responsible for significant misfit and try to reduce these regions first.
2. We anticipate multiple misfit regions associated to each smooth shape. The most complicated element in a misfit description is the representation of the outermost 1D boundary of the misfit. We use the outermost 1D boundary to define a Riemann sum approximation to the misfit. Consequently, we will ignore (initially, at least) low amplitude but high frequency nearby features.
3. Define height field (relative to the smooth approximant) contours at each critical point in the noisy implicit surface. Project these contours onto the smooth approximant.
4. Smooth the set of projected contours. For each contour in the parameterization we identify the critical points on that contour. We triangulate the annular region bounded between consecutive contours.
5. Now we fit a frustum-like collar to the base of the region where the misfit attaches to the background.
6. The cumulative shape resembles a telescope, hence the name "telescopic deformation". The process accommodates tendril-like shapes, in

the sense that surfaces can recursively support branches off other earlier branches.

Figures 28a-c illustrate an example of the misfit reduction process. Suppose that we want to reduce the misfit in approximating a tendril shape by a plane, see Figure 28a. We subdivide the tendril using height field planes that approximately set to the tendril's critical points.

10 We have generated a sequence of truncated collars that reduce the misfit. We are not done, however, since this approximation is not differentiable at any point on a collar ring separating two truncated cones. We remedy this deficiency by replacing a thin swath about the ring
15 with a thin swath about the equator of a sphere.

Figures 29a-c illustrates an example of blending a non-differentiable join of two collars. The idea is to map given instance (Figure 29a) to the one situation that we understand how to fix (Figure 29b). The one situation
20 that we understand how to fix is an isosceles right triangle with an inscribed circle such that the center of the circle is the centroid of the triangle. We apply the linear transformation shown in Figure 29c to the isosceles right triangle in panel shown in Figure 29b to
25 the exterior and interior triangles - corresponding to θ_1 and θ_2 , respectively - in Figure 29a.

The misfit reduction procedure is as follows.

1. We construct height field contours on the noisy
30 surface S . Remember that the height field is taken normal to the smooth shape approximation S^* .

2. Working top down, we project each contour to S^* . It is possible that the projection of successive contours cross.
3. We approximate each contour projection in two steps.
 5 First we locate all 1D critical points - minima, maxima, and inflection points. Second we fit a smooth approximation to each section of the projected contour; where a section is delimited by critical points.
- 10 4. We triangulate the interior of each projected contour, and then construct tetrahedra using consecutive contours.
5. We approximate the cap/cup corresponding to the innermost ring of the bull's eye with the ring's
 15 closure in the plane.

We next consider how to describe a branching structure of hills that separate a region into multiple valleys. Figure 30 shows as a geological example a water
 20 breach as indicated by the white arrow.

Here is a compact description of this branching structure.

1. Find the ridge edge in the branching structure. The
 25 ridge edge is a connected (therefore degenerate) set of critical points.
2. We assume that as typical cross section is a conic section, e.g., a parabola, an ellipse, etc.
3. We allow for stretching and contracting of the cross
 30 section. We call a region over which the typical cross section stretches or contracts a "transition zone". We provide linear interpolation between the start and stop position cross sections.

4. We anticipate a valley that runs perpendicularly to the ridge edge. For the case of a branching structure, we treat a valley of this type as a misfit. The following NASA aerial reconnaissance image contains active breaches in the ridge structure.

We consider a more challenging example. Figure 31 is a NASA Shuttle Mission photograph of the Richat Structure in Mauritania. NASA believes that most likely explanation of the origin of this structure is that it is uplifted rock sculpted by erosion. NASA also says that there is no widely accepted theory that explains why the Richat Structure is nearly circular.

The dominant shape in the Richat Structure is a nested sequence of toroidal structures. Because of erosion, some of the toroidal structures exist as sections of a torus only. Ecker argues on pg. 4-5 of his lecture notes that a torus satisfies mean curvature flow with respect to its mean curvature. This flow is singular, in the sense that in finite time the circular cross section shrinks to a point and hence the torus shrinks to a circle. This is a second example of the fact that mcf evolution need not preserve the dimension of a shape. (The other example is an uncapped cylinder whose radius $r(t)$ is given by the formula

$$r(t) = \sqrt{r^2(0) - 2t}, \text{ provided that } t \in (0, \frac{r^2(0)}{2}).$$

In finite time the

uncapped cylinder collapses to its axis of symmetry.

With respect to known techniques, Rouby et al. describe a parameterization algorithm for triangulated surfaces. See, D. Rouby, H. Xiao, J. Suppe, 3D Restoration of Completely Folded and Faulted Surfaces

Using Multiple Unfolding Mechanisms, AAPG Bulletin 84(6), June 2000, pg. 805-829. This method involves projecting the triangulation onto the (x,y) co-ordinate plane. It is not clear how to compensate for triangles that have a
 5 near singular projection. Also, the projection of multiple triangles onto a common plane can lead to a complicated overlapping and slivers. These are the sort of numerical instabilities that we want to avoid and which this algorithm does avoid.

10

A description will now be give for 3D conformal grid generation and reconstruction of shape from disconnected pieces, according to the invention.

Shape identification improves the performance of our
 15 incremental 3D conformal grid generator. Given a sub-volume V with boundary $\partial V = S$, we uniformly approximate S as a collection of trimmed ideal elementary shapes $\{E_m\}$. Then we enclose S in a tight sequence of rectangular prisms $\{P_k\}$ such that the "vertical" edges of the prism
 20 are normal to the ideal elementary shape approximants.

We generate a 3D conformal grid in 3 parts.

1. $\partial P_k \cap S$, which is the part between the prism faces
 25 and the measured surface S .
2. The bounding box B_m of each trimmed ideal elementary shape E_m .
3. A prism $P^* \subseteq V$ such that $P^* \cap B_m = \emptyset$.

30 We use a proportional spacing correlation scheme to grid part #1. In part #2 we use E_m 's parametric expression for normals to grid B_m . In part #3 we grid P^* in the obvious way. The incremental nature of the

procedure follows from the subdivision of the grid into regions associated with the prismatic enclosure of S and the uniform approximation by trimmed ideal elementary shapes.

5 Figure 32 shows a conformal grid induced from a proportionally spaced correlation scheme. We use a proportional spacing correlation scheme to define the grid iso-surfaces. Here is an ideal application of this mechanism (This is an idealization of a cross section
10 through the Gullfaks field.). We see that the sub-blocks have approximately the same z-direction thickness. It is irrelevant how the horizontal extents correspond. In other words, we can generate either a regular spacing grid or an irregular spacing grid. We remark that a
15 compromise such as a "tartan grid" (also known as a rectilinear grid) is more memory efficient than a regular grid but still has a convenient algebraic lookup function.

 We observe that a correlation scheme implements a
20 cheap form of mean curvature flow and if generated independently of a parameterization, then the conformal grid is a roundabout way to also generate a parameterization.

25 We conclude this part of the description with a discussion of a way to convert an existing 3D Cartesian grid to a conformal grid. Figure 33 illustrates a non-conformal 3D Cartesian grid. As is well known, it is non-trivial to trim grid cells that cross volume boundaries.
30 Here the background grid shown in dashed lines, crosses the overburden. It is clear in this diagram that the background grid cells do not conform to lithological boundaries.

We remedy these deficiencies in the following way.

1. We attach the volume of interest to a spatial frame.
- 5 2. We conformally grid the volume that lay between the overburden and the reservoir.
3. For best results we want a transition zone from a Cartesian grid to the conformal grid, preventing reverberation in the grid across lithological boundaries.
- 10

Forensic reconstruction will now be discusses.

Suppose that an application identifies a set of disconnected 2D patches and would like to construct a surface from the patch set. We show how mean curvature flow enables us to construct such a surface - hence the sub-title for this discussion. This technique will be seen to be similar in execution to grid generation, which is why we discuss it here.

20 Suppose that we have a collection of 2D patches in R^3 . We assume that all of the patches are oriented in a consistent manner, which must be the case if all of the patches are taken from a common surface. We construct the solution using patches or parts of patches that have a common Gaussian curvature signum. We do not insist that the Gaussian curvature signum be constant across the patch point set. However, if it is not constant, then we use only those patches and parts of patches that have the same signum to construct a surface. This procedure can create holes in the surface. We fill in these holes with the remainder of patches that were used only partially. Some patches with the opposite signum may not fill in holes, but instead form folds in the surface. We

25

30

construct a second surface from these patch point sets and union the two parts together.

We remark that the following algorithm is applicable to the task of sewing together parts of the bounding
5 surface of a geobody, e.g., a salt body.

Our method is as follows.

1. We assume that the velocity of the flow equals 1, so
10 that a time interval is equal to a distance.
2. For each patch or region of a patch R that has (+) signum Gaussian curvature, we define a uniformly expanding mean curvature flow with initial condition equal to R .
- 15 3. These patches are taken from a common surface, so we sample each flow at the same time step increments.
4. We stop a particular flow when it intersects another flow pattern.
5. Eventually each flow intersects a different flow.
- 20 6. It may be that the confluence of two flows is not differentiable. If this happens, then we define a flow to smooth the sharp angle. Alternatively, we can smooth the sharp angle using the Squeeze operator defined in the Misfit Reduction
25 algorithm.

If a formation contains a tunnel, then we may wish to reverse the dissolution process, i.e., fill in the tunnel. In this situation we will approximate the tunnel
30 as a collection of uncapped cylindrical and toroidal sections. Ecker's lecture notes show that mean curvature flow applied to an uncapped cylinder will shrink the 3D surface onto its 1D axis of symmetry in finite time. Smoczyk has obtained a comparable result for a torus. His
35 result shows that a torus collapses under mean curvature

flow to its inner parabolic circle in finite time. We conclude that when applied to a tunnel, mean curvature flow will collapse the tunnel to a curve in finite time.

Figure 34 is an image of the Devil's Potholes, South Africa. We can identify two different kinds of pothole formations in this image. The circled pothole on the right is well described as a cylinder. We can collapse it to its axis of symmetry - which is a line - under mean curvature flow. The pothole on the left is more complex. The top of this region is a curved throat, which is followed by a sharp edged cone. Finally there is a toroidal section that is turning away from the viewer. We know that each section will collapse to a singular edge in a finite amount of time. Taking the longest time interval needed to collapse a section of this structure, we guarantee that the entire pothole will collapse to a polygonal path.

We now discuss a related problem. Given an image of a layered sequence, suppose that an unconformity. The unconformity will erase everything in the image that is above the unconformity. How good a reconstruction of the eroded interface can I achieve, given just the migrated image. As an example, we return to the diagram of a cross section of a shallow sequence in Turkmanistan shown in Figure 3. We are interested in the guess of what the missing section of the layer looks like.

Our algorithm assumes that the formation satisfies the following assumptions.

1. There exists a reference layer such that the visible part of the sequence is well approximated by a single reference surface adaptively sampled

correlation scheme. In the above schematic, the vertically striped layer R is the reference layer.

2. We reconstruct the eroded region of a layer by evolving the reference interface under mean curvature flow until the front joins the unconformity. In the above schematic, the reconstructed interfaces are shown as dotted outlines above the unconformity.

10

While it may not be obvious from Figure 3, conformal grid generation is a very short time solution to mean curvature flow. In other words, if erosion had not been imposed then we would recognize the conformal grid generation in the framework close to the reference surface and flattening further away. As an illustration, we consider Figure 35, which is a NASA LANDSAT image of the Yukon River delta (NASA Geomorphology plate D-9). We focus on the boundary cracks that subdivide the rounded joint at the left top of the image. These boundaries delimit curvature flow regions that collectively form the bend in the deltaic mass. It has been proposed to use a diffusive process. See, J. Davis, S. Marschner, M. Garr, M. Levoy, Filling holes in complex surfaces using volumetric diffusion, First International Symposium on 3D Data Processing, Visualization, and Transmission, Padua, Italy, June 19-21, 2002. This reference does not make use of curvature information in the algorithm used. Furthermore, the reference does not deal with closing 3D voids such as tunnel closure.

30

We have discussed how to construct a patchwork covering of an implicit surface from first order Taylor polynomials. The error term is quadratic with coefficients that are the principal curvatures defined at a point that is somewhere within the circle of convergence about the expansion point. The radius of the circle is chosen so that the error term is smaller than a user-defined tolerance. The error estimate is not sharp, because it is not obvious where to evaluate the error term's principal curvature values, i.e., what is the definition of α . Since this error estimate is not sharp, we supplement the Taylor representation with a fast technique to evaluate α .

From curvature analysis we derive a representation of a surface as a connected sum of trimmed elementary shape. Some examples of elementary shapes are (sections of) an ellipsoid, hyperboloid, cyclide, and a prism. An elementary shape has algebraic expressions for mean curvature and Gaussian curvature. These expressions can be substituted into the quadratic formula to generate an algebraic expression for principal curvature. Unfortunately the resulting expression is often so complex algebraically that a symbolic algebra package such as Mathematica® must be used for any manipulation other than simple evaluation. This is awkward in an Engineering environment, so a low order Taylor series approximation is preferable.

Here is an intersection algorithm for implicit surfaces. This algorithm assumes that every surface's signed distance function has been defined on a shared grid.

Notation

S_1 implicit surface #1

σ_1 a point on S_1

5 τ_1 parametric definition for σ_1

S_2 implicit surface #2

σ_2 a point on E_2

τ_2 parametric definition for σ_2 .

10

G a shared 3D grid

C a grid cell in G such that $C \cap S_1 \cap S_2 \neq \emptyset$

c_i a point in $C \cap S_1 \cap S_2$.

σ_{12} a point in $C \cap S_1 \cap S_2$.

15

Intersection algorithm

1. Find all grid cells $\{C_k\}$ that surface S_i intersects.
A grid cell is involved if and only if the signed
20 distance function is not constant at all grid cell
corners.

2. In this algorithm we want to work with surface
patches that project invertibly onto a face of grid
cell. We subdivide the part of a surface contained
25 in a grid cell into the desired patchwork by
checking the surface normal field restricted to the
grid cell. We place a point on the surface in a
patch exactly when the unit normal at the point is
within tolerance of being parallel to all other
30 surface points that are already assigned to the
patch.

For each S_1 patch find all S_2 patches such that their
corresponding sdf patterns do not rule out intersection.

For clarity we assume that each surface contains exactly one such patch.

Loop\$0:

5

3. Let c_0 be the midpoint of the line segment λ_0 connecting two faces of C such that the signum of the sdf for S_1 on one of the connected faces is different from that on the other.

- 10 4. Let $j = 0$.

Loop\$1:

5. Project c_j onto S_1 and S_2 , respectively.
- 15 6. Label the projection s_{1j} and s_{2j} , respectively.
7. Either $s_{1j} = s_{2j}$ or not.
8. If $s_{1j} = s_{2j}$, then go to **Label\$2**.
9. If $s_{1j} \neq s_{2j}$, then construct the line segment λ_{j+1} in C_k connecting s_{1j} to s_{2j} .
- 20 10. Let c_{j+1} be the midpoint of λ_{j+1} .
11. It might be the case that $c_j \approx c_{j+1}$. We expect to see this when a very thin hyperbolic neck is contained in the same cell as C_k .
12. If $c_j \approx c_{j+1}$, then we want to jump away from this
- 25 hopeless local minimum. We do this by comparing the signum of the sdf for s_{1j} and the signum of the sdf for s_{2j} to signum of sdf obtained on the grid cell faces joined by the line segment λ_0 . Moving in the direction that differs from the current values, jump
- 30 to the midpoint along λ_0 .
13. Increment j and return to **Loop\$1**.

Label\$2:

We use a Newton algorithm to find another point of intersection.

Loop\$3:

5

14. Let (x_{12}, y_{12}) be a point of intersection for S_1 and S_2 in C and suppose that (x_{12}^*, y_{12}^*) is another point of intersection in C . Expanding each surface in a 1st order Taylor series about (x_{12}, y_{12}) , we have

10

$$\begin{aligned} S_1(x_{12}^*, y_{12}^*) &= S_1(x_{12}, y_{12}) + \nabla S_1(x_{12}, y_{12}) \cdot (x_{12} - x_{12}^*, y_{12} - y_{12}^*) \\ S_2(x_{12}^*, y_{12}^*) &= S_2(x_{12}, y_{12}) + \nabla S_2(x_{12}, y_{12}) \cdot (x_{12} - x_{12}^*, y_{12} - y_{12}^*) \end{aligned}$$

15. Subtracting, we have 2 linear equations in two unknowns. Solve for the non-trivial solution

15

$$0 = \nabla (S_2 - S_1)(x_{12}, y_{12}) \cdot (x_{12} - x_{12}^*, y_{12} - y_{12}^*)$$

16. Return to **Loop\$3** until (x_{12}^*, y_{12}^*) is acceptably close to being another point of intersection in C .

20

17. We compute the intersection curve between (x_{12}, y_{12}) and (x_{12}^*, y_{12}^*) by repeating the midpoint subdivision algorithm in **Loop\$2**.

18. Return to **Loop\$3** and repeat the 1st order Taylor series algorithm in **Loop\$2** on both ends (x_{12}, y_{12}) and (x_{12}^*, y_{12}^*) until the curve crosses the faces of C_k .

25

19. Return to **Loop\$3** and continue processing grid cells in $\{C_k\}$ until exhaustion.

Visualization of an intersection curve is as follows.

30

1. Project the intersection curve onto the internal cylindrical parameter space.
2. Facet the cylinder using a constrained Delaunay algorithm.

3. Invert the mapping, projecting the triangulation of the region enclosing the "flattened" intersection curve to the parent implicit surface.

5 We have described a curvature-adaptive method for placing sample points on a surface and generating a narrow band octree from them. Now we discuss how spatial frames can be used to implement an efficient update mechanism. For details of the reappearance of SIGMA's
10 hybrid grid-mesh concept, refer to U.S. Patent Application Serial No. 09/163,075, incorporated herein by reference.

Each geological feature has its own octree which overlays part of the background octree. An overlay can
15 cover a strictly smaller region of the background, and this small region can be sampled differently (adaptively) from the background. The sampling can be adapted to the complexity of the framework region that the overlay encloses. The overlay changes as the framework region
20 changes. A separate spatial frame is assigned to control each octree overlay. Overlays are loaded on demand. Within a spatial frame the sampling can be adjusted in an adaptive manner. A frame boundary sample node can be part of multiple octree overlay. An entity that is outside a
25 particular spatial frame learns about the frame's enclosed shape by interrogating the enclosing spatial frame. Given an octree identifier and a location inside or on the boundary of the octree's enclosing frame, the local cpt returns the cpt and sdf for the remote octree
30 overlay. Adjacent frames might support a different set of and number of framework surfaces.

Given a region of interest, we associate to each spatial frame the point set that the frame contains. We

represent the set of spatial frames associated with a region of interest as a directed acyclic graph. Two parent frames that partially overlap will be represented in the graph as nodes that point to a common descendant.

5 Thus spatial frames constitute a topology graph.

As an example, a vsp was acquired over part of the Zechstein Salt formation. Figures 36a and 36b show, for reference, the background Zechstein Salt and the region in the Zechstein where the vsp was acquired. Figure 37
10 show the frame graph that ties the vsp region of interest to the Zechstein Salt background. We use the inner frame to outer frame relationship to express "A is a boundary of B" and "A is logically part of B". In GQI terminology a spatial frame as defined herein is equivalent to a
15 `gqi_Frame_t`. We have extended this functionality two ways. First, we maintain logical containment, i.e., feature relationships. Second, we allow mixing space and time frames.

Spatial frames are useful in subdividing a faulted
20 region to match regions subject to different physics. For example, Figures 38a, 38b, 39a and 39b illustrate the separation of faulted sediments from unfaulted sediments. Figure 38a and 38b show the case of a sequence of sediments such that some but not all of the sediments
25 have been faulted, and a simple normal fault is involved. Figures 39a and 39b show the case of a fault network where some of the faults in the network emanate from other faults. Figure 39b shows that the unique final configuration of spatial frames that partition the
30 volumes shown in Figure 39a. Using mathematical induction on the number of faults in a compact region of interest, we conclude that it is immaterial in what order

spatial frames are assigned to isolate distinct sedimentary regions. In other words, the final subdivision is always the same no matter what the order of isolation is.

5 We think of mean curvature flow as an evolutionary process. For simplicity, we assume that any evolutionary process is a structure group of diffeomorphisms of some 4D fibre bundle. All information regarding the process at a moment in time is encoded in a time frame. A time frame
10 contains a reference to a region of interest that in turn is represented as a 3D fibre bundle. We do not demand that an evolutionary process provide a physically plausible explanation of a formation state, rather it is enough if the visual expression appears plausible.

15 Figure 40 illustrates a time-lapse seismic evolution (steam injection front tracking, with the left panel "before" and the right panel "after"). We discuss now how we use spatial frames to define a topology graph. Let S be an implicit surface and let $\{E_k\}$ be a family of
20 elementary shapes that approximate S . Each E_k reduces its misfit with S by fitting a disjoint region of S to a telescopic extrusion of E_k .

We use a different spatial frame to contain each telescopic extrusion and attach the collection of these
25 frames. We assign each elementary shape to its own spatial frame and refer to the misfit reduction through attachment of the spatial frame list to the parent elementary shape frame. Figure 41 shows the reference structure for this set of relationships.

30

We summarize the contents of the new class instances that we have defined in this paper.